HEAT CONDUCTION IN ELASTIC SYSTEMS: FOURIER VERSUS CATTANEO

Racke, R.
Department of Mathematics and Statistics,
University of Konstanz,
78457 Konstanz,
Germany,
E-mail: reinhard.racke@uni-konstanz.de

ABSTRACT

The classical model for heat conduction using Fourier's law for the relation between the heat flux and the gradient of the temperature qualitatively yields exponentially stable systems for bounded reference configurations. This kind of stability remains the same if one replaces Fourier's law by Cattaneo's (Maxwell's,...) law. Considering thermal and, simultaneously, elastic effects, this similarity with respect to exponential stability remains the same for classical second-order thermoelastic systems, one being a hyperbolic-parabolic coupling, the other being a fully hyperbolic system. The similarities even extend to the asymptotical behavior of solutions to corresponding nonlinear systems. But for thermoelastic plates, a system of fourth order and being one of recently found examples, the picture changes drastically, i.e., this thermoelastic system changes its behavior from an exponentially stable to a non-exponentially stable one, while changing Fourier's law to Cattaneo's law. This raises the question of the "right" modeling.

We present a large class of general systems with this behavior demonstrating that it might be more likely that Fourier and Cattaneo predict different qualitative behavior in thermoelastic systems. For this purpose we consider a coupled system depending on a family of parameters, a special case of which describes the thermoelastic plates above, where in only one singular case of the parameters the exponential stability property is kept while replacing Fourier by Cattaneo - and lost in all other cases. Interestingly, the singular case corresponds to the second-order thermoelastic system mentioned above.

We use methods from functional analysis for proving the loss of exponential stability in the Cattaneo case.

INTRODUCTION

The simplest classical equations of heat conduction for the temperature difference $\theta = \theta(t,x) = T(t,x) - T_0$, where T denotes the absolute temperature and T_0 is a fixed constant reference temperature, and for the heat flux $q = q(t,x)$, and putting constants equal to one w.l.o.g, are given by

$$\begin{aligned} \theta_t(t,x) + \operatorname{div} q(t,x) &= 0, \qquad t \geq 0,\ x \in \mathbb{R}^n, \qquad (1) \\ q(t,x) + \nabla\theta(t,x) &= 0, \qquad \text{(Fourier's law)}. \qquad (2) \end{aligned}$$

Combining (1) and (2) yields the parabolic heat equation

$$\theta_t(t,x) - \Delta\theta(t,x) = 0. \qquad (3)$$

Observation: Model (3) predicts an infinite speed of propagation of signals.

If one replaces Fourier's law (2) by Cattaneo's (Maxwell's, Vernotte's,...) law,

$$\tau\, q_t(t,x) + q(t,x) = -\nabla\theta(t,x), \qquad (4)$$

with a small relaxation parameter $\tau > 0$, and if we combine now (1) with (4) we obtain the hyperbolic damped wave equation

$$\tau\theta_{tt}(t,x) + \theta_t(t,x) - \Delta\theta(t,x) = 0. \qquad (5)$$

Observation: Model (5) predicts a finite speed of propagation of signals.

As it is well known solutions to the classical heat equation equation (3) and to the classical damped wave equation (5) qualitatively show the same behavior: In bounded reference configurations Ω, with, for example, zero boundary conditions for θ modeling constant temperature T_0 at the boundary, we have exponential stability of the system as time tends to infinity:

$$\int_\Omega \theta^2(t,x)\,dx \leq C\,\mathrm{e}^{-dt}$$

for some positive constants C, d. E.g. for solutions to (3), we have

$$\int_\Omega \theta^2(t,x)\,dx \leq \tilde{C}\,\mathrm{e}^{-dt} \int_\Omega \theta^2(0,x)\,dx$$

with a constant $\tilde{C}$ being independent of the data $\theta(0,\cdot)$ at time zero ($\tilde{C}$ depends on the domain Ω, essentially on the smallest eigenvalue of the negative Dirichlet-Laplace operator $-\Delta_D$ realized in L^2).

We remark that if we replace the bounded reference configuration Ω by all of $\mathbb{R}^n$ or by an exterior domain, we have similar polynomial (only) decay instead of exponential decay for the L^2-norm or, for example, uniformly in x :

$$\sup_{x\in\mathbb{R}^n} |\theta(t,x)| \leq C\,t^{-n/2}.$$

Now taking into account both elastic and thermal effects, in a bounded reference configuration in one space dimension like $\Omega = (0,1)$, we consider the classical system

of thermoelasticity, where $u = u(t,x) = X(t,x) - x$ denotes the displacement (with position $X(t,x)$ at time t for the particle x in the fixed reference configuration Ω), and where again most constants are set equal to one,

$$\begin{aligned} u_{tt} - u_{xx} + \theta_x &= 0, \\ \theta_t + q_x + u_{tx} &= 0, \\ \tau q_t + q + \theta_x &= 0. \end{aligned} \tag{6}$$

Typical boundary conditions are $u(t,0) = u(t,1) = 0$ and $\theta(t,0) = \theta(t,1) = 0$ on the boundary of Ω, modeling the situation where the boundary is kept fixed and where the temperature is again kept constantly equal to the reference temperature T_0.

The qualitative behavior is the same for $\tau = 0$ (Fourier) and for $\tau > 0$ (Cattaneo): As time tends to infinity, the energy tends to zero exponentially. Here the energy at time t means the expression

$$\int_0^1 (u_t^2 + u_x^2 + \theta^2 + q^2)(t,x)\, dx$$

involving kinetic and potential energy in terms of u as well as thermal energy expressed in terms of θ and q.

Even the *quantitative* behavior is similar: Replacing (6) by the corresponding equations with real physically given material constants for different real materials, the optimal $\alpha > 0$ in

$$\int_0^1 (u_t^2 + u_x^2 + \theta^2 + q^2)(t,x)\, dx \le C\, \mathrm{e}^{-\alpha t}$$

is similar for materials like silicon, aluminum alloy, steel, germanium, gallium arsenide, indium arsenide, copper and diamond [1]. Similarities also extend to corresponding nonlinear systems.

These observations of similar behavior raises the impression that both heat conduction models, the Fourier model or the Cattaneo model, lead to the same qualitative (or even quantitative) behavior.

We will present examples with essentially different qualitative behavior, where the system is exponentially stable for the Fourier model, and not exponentially stable for the Cattaneo model. This raises the question of the "right" modeling. We start with models for thermoelastic plates, a system of fourth order in the space variable, and mention a Timoshenko type system where the Cattaneo model even "destroys" an exponential stability given in the model without heat conduction, or with heat conduction modeled by Fourier's law. As main part and new contribution, we present a large class of more general coupled systems with this different behavior. For this purpose we consider a coupled system depending on a family of parameters, a special case of which describes the thermoelastic plates above, where in only one singular case of the parameters the exponential stability property is preserved while replacing Fourier by Cattaneo - and lost in all other cases. This demonstrates that it might be more often that Fourier and Cattaneo predict different qualitative behavior in thermoelastic systems.

The singular case where exponential stability is true for both models corresponds to the second-order thermoelastic system (6).

THERMOELASTIC PLATES

A Kirchhoff type thermoelastic plate can be modeled in a bounded reference configuration $\Omega \subset \mathbb{R}^n$ by the following three equations

$$\begin{aligned} u_{tt} + a\,\Delta^2 u + b\,\Delta\theta &= 0, \\ \theta_t + c\,\mathrm{div}\, q - d\,\Delta u_t &= 0, \\ \tau q_t + kq + \nabla\theta &= 0, \end{aligned} \tag{7}$$

where $u = u(t,x)$ denotes the displacement, $\theta = \theta(t,x)$ the temperature difference, and $q = q(t,x)$ the heat flux again, and a, b, c, d, k are positive constants. For suitable boundary conditions, i.e. the hinged boundary conditions $u(t,\cdot) = \Delta u(t,\cdot) = 0$ on the boundary of Ω, the system is exponentially stable for $\tau = 0$ [3, 4, 5, 6], but not for $\tau > 0$ [7, 8]. That is, the asymptotic behavior for the different models is, surprisingly, essentially different.

We remark that on a formal level *exponential stability of a system* means that, after rewriting the differential equations as a first-order system in time for some vector function $V = V(t,x)$,

$$V_t(t,\cdot) + \mathbb{A}V(t,\cdot) = 0,$$

the semigroup $\{\mathrm{e}^{-\mathbb{A}t}\}_{t\ge 0}$ generated by the differential operator $\mathbb{A}$ acting in the x-variable and being defined in some Hilbert space H is an exponentially stable semigroup. The latter now means that there is a number $\alpha > 0$ and a constant $C_0 > 0$ such that for all initial data V_0 in H, and for all $t \ge 0$ one has

$$\|\mathrm{e}^{-\mathbb{A}t} V_0\|_H \le C_0\, \mathrm{e}^{-\alpha t} \|V_0\|_H.$$

TIMOSHENKO BEAMS

In models for beams of Timoshenko type, a given exponentially stability triggered by a typical memory (history) term, is preserved by adding heat conduction in form of the Fourier model, but is lost – hence "destroyed" – by the Cattaneo model. The four differential equations in the model are given by

$$\begin{aligned} \rho_1 \varphi_{tt} - k(\varphi_x + \psi_x)_x &= 0, \\ \rho_2 \psi_{tt} - b\psi_{xx} + \int_0^\infty \mathrm{e}^{-s} \psi_{xx}(t-s,\cdot)\, ds + & \\ k(\varphi_x + \psi) + \delta\theta_x &= 0, \\ \rho_3 \theta_t + q_x + \delta\psi_{tx} &= 0, \\ \tau q_t + dq + \theta_x &= 0. \end{aligned}$$

Here, the functions ϕ and ψ model the transverse displacement of a beam with reference configuration $(0,1)$ respectively the rotation angle of a filament. θ and q denote again the temperature difference and the heat flux, respectively. The material constants $\rho_1, \rho_2, k, b, \delta, \rho_3, d$ are positive, as well as the already introduced relaxation parameter τ. The

term $\int_0^\infty e^{-s}\psi_{xx}(t-s,\cdot)ds$ models the additional consideration of the history.

Assuming the (academic, in general physically not satisfied) condition

$$\frac{\rho_1}{k} = \frac{\rho_2}{b},$$

which corresponds to the equality of the wave speeds for ϕ and ψ, we have the following picture:

For $\delta = 0$, it is a hyperbolic system with history term for (ϕ, ψ), and exponential stability is given. For the coupled system with $\delta \neq 0$ and $\tau = 0$ (Fourier), the exponential stability is preserved. But for $\delta \neq 0$, $\tau > 0$ (Cattaneo), the exponential stability is lost [2]. Again the question of an appropriate modeling comes up.

α-β-SYSTEMS

We now present a new, larger class of coupled systems where the same effect shows up – exponential stability under the Fourier law, and no exponential stability under the Cattaneo law. It will appear as an abstract α-β-system (10), with parameters $0 \leq \alpha, \beta \leq 1$, for functions $u, \theta : [0,\infty) \to \mathcal{H}$ into a Hilbert space $\mathcal{H}$.

The case $\tau = 0$ has been studied before:

$$\begin{aligned} u_{tt}(t) + aAu(t) - bA^\beta\theta(t) &= 0, \\ \theta_t(t) + cA^\alpha\theta(t) + dA^\beta u_t(t) &= 0. \end{aligned} \tag{8}$$

Here A denotes a self-adjoint operator with countable system of eigenfunctions $(\phi_j)_j$ with corresponding increasing eigenvalues $0 < \lambda_j \to \infty$ as $j \to \infty$. The constants a, b, c, d are positive.

The example of the thermoelastic plate (7) is, for $\tau = 0$, a special case with

$$\alpha = \beta = \frac{1}{2}, \quad A = (-\Delta_D)^2,$$

where $-\Delta_D$ denotes the Dirichlet-Laplace operator with zero (Dirichlet) boundary conditions realized in L^2. The case $\alpha = 1$, $\beta = \frac{1}{2}$ corresponds to the second-order thermoelastic system (6), and with the case $\alpha = 0$, $\beta = \frac{1}{2}$ one can model a viscoelastic system [9].

This system was introduced in [9, 10]. The most detailed recent discussion concerning exponential stability, smoothing properties and more can be found in [11, 12]. Exponential stability is known for (8) in the striped region

$$\mathcal{A}_{es}(\tau = 0) := \{(\beta, \alpha) \,|\, 1 - 2\beta \leq \alpha \leq 2\beta, \alpha \geq 2\beta - 1\}, \tag{9}$$

see Figure 1.

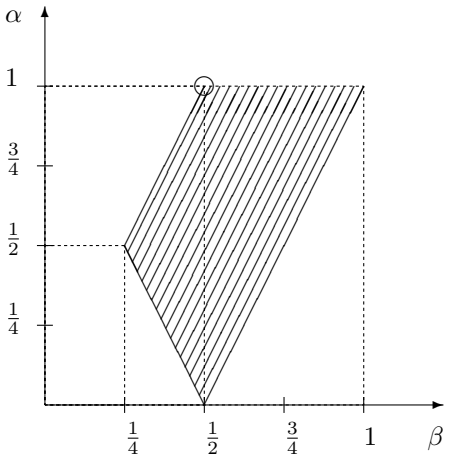

Figure 1: $\mathcal{A}_{es}(\tau = 0)$

The pair $(\beta, \alpha) = (\frac{1}{2}, 1)$ is highlighted by a circle since this will be the only pair for which the exponential stability will remain true if we replace the Fourier law by the Cattaneo law in (10). In the remaining part of the striped region of exponential stability for $\tau = 0$, the property of exponential stability will be lost, see Theorem 1 below.

The abstract Cattaneo version corresponding to the Fourier version (8) is given by

$$\begin{aligned} u_{tt}(t) + aAu(t) - bA^\beta\theta(t) &= 0, \\ \theta_t(t) + B_1 q(t) + dA^\beta u_t(t) &= 0, \\ \tau q_t(t) + q(t) + B_2\theta(t) &= 0, \end{aligned} \tag{10}$$

with abstract operators B_1, B_2 satisfying

$$-B_1 B_2 = cA^\alpha. \tag{11}$$

Here, $u, \theta : [0,\infty) \to \mathcal{H}$, and $q : [0,\infty) \to (\mathcal{H})^m$ for some $m \in \mathbb{N}$. The operator B_2 maps its domain in $\mathcal{H}$ into $(\mathcal{H})^m$,

$$B_2 : D(B_2) \subset \mathcal{H} \to (\mathcal{H})^m,$$

and

$$B_1 : D(B_1) \subset (\mathcal{H})^m \to \mathcal{H}.$$

The thermoelastic plate model (7) is contained choosing realizations of the divergence operator "$c\,\mathrm{div}$" for B_1, and of the gradient operator "∇" for B_2, and $m = n$ in $\mathbb{R}^n$.

The exponential stability given for the Fourier model (8) and described by $\mathcal{A}_{es}(\tau = 0)$ in Figure 1, is lost for the Cattaneo model in any point different from $(\beta, \alpha) = (\frac{1}{2}, 1)$.

Theorem 1 *The region of exponential stability given for the Fourier model by $\mathcal{A}_{es}(\tau = 0)$ in (9) resp. Figure 1, is lost for the system (10) in any point different from the singular point $(\beta, \alpha) = (\frac{1}{2}, 1)$ which corresponds to (6).*

Proof: The exponential stability of system (10) for $(\beta, \alpha) = (\frac{1}{2}, 1)$ (and $\tau > 0$ from now on) has been proved for the realization (6) for various boundary conditions [13].

We shall prove the *non*-exponential stability for the remaining values of $(\beta, \alpha) \in \mathcal{A}_{es}(\tau = 0)$. As ingredients of the proof we have an eigenfunction expansion and the Hurwitz criterion. For the proof we may assume for simplicity,

but w.l.o.g., that the constants a, b, c, d appearing in (10), (11) satisfy $a = b = c = d = 1$.

The idea is to use the following ansatz of separation of variables via the eigenfunctions $(\phi_j)_j$ of A,

$$u_j(t) = a_j(t)\phi_j,\ \theta_j(t) = b_j(t)\phi_j,\ q_j(t) = c_j(t)B_2\phi_j, \quad (12)$$

for arbitrary j (assuming $B_2\phi_j$ not being identically zero), and to find solutions with decay contradicting exponential stability.

Using (11) we observe

$$B_1 q_j(t) = c_j(t)B_1B_2\phi_j = -c_j(t)A^\alpha\phi_j = -\lambda^\alpha c_j(t)\phi_j,$$

thus solving (10) is equivalent to solving the following system of ODEs for the coefficient functions (a_j, b_j, c_j), where a prime $'$ denotes differentiation with respect to time t,

$$\begin{aligned} a_j'' + \lambda_j a_j - \lambda_j^\beta b_j &= 0, \\ b_j' - \lambda_j^\alpha c_j + \lambda_j^\beta a_j' &= 0, \\ \tau c_j' + c_j + b_j &= 0. \end{aligned} \quad (13)$$

The last equation arises from the last equation in (10) with the ansatz (12) using again the natural condition that $B_2\phi_j$ is not identically zero.

System (13) is equivalent to a first-order system for the column vector $V_j := (a_j, a_j', b_j, q_j)$,

$$V_j' = \begin{pmatrix} 0 & 1 & 0 & 0 \\ -\lambda_j & 0 & \lambda_j^\beta & 0 \\ 0 & -\lambda_j^\beta & 0 & \lambda_j^\alpha \\ 0 & 0 & -\frac{1}{\tau} & -\frac{1}{\tau} \end{pmatrix} V_j \equiv A_j V_j. \quad (14)$$

We are looking for solutions to (14) of type

$$V_j(t) = \mathrm{e}^{\omega_j t} V_j^0.$$

In other words, ω_j has to be an eigenvalue of A_j with eigenvector V_j^0 as initial data.

It is the aim to demonstrate that, for any given small $\varepsilon > 0$, we have some j and some eigenvalue ω_j such that the real part $\Re\omega_j$ of ω_j is larger than $-\varepsilon$. This will contradict the exponential stability (being a kind of uniform property over all initial values), observing

$$|V_j(t)| = \mathrm{e}^{\Re w_j}|V_j^0|.$$

Computing the characteristic polynomial of A_j we have

$$\begin{aligned} \det(A_j - \omega) &= \frac{1}{\tau}\left(\tau\omega^4 + \omega^3 + \left[\lambda_j^\alpha + \tau(\lambda_j + \lambda_j^{2\beta})\right]\omega^2 \right. \\ &\quad \left. + [\lambda_j + \lambda_j^{2\beta}]\omega + \lambda_j^{1+\alpha}\right) \\ &\equiv \frac{1}{\tau}P_j(\omega). \end{aligned}$$

To reach our aim, i.e. to show that

$$\forall\,\varepsilon > 0\ \ \exists\, j\ \ \exists\,\omega_j,\ P_j(\omega_j) = 0 :\ \ \Re\omega_j \geq -\varepsilon,$$

we introduce, for small $\varepsilon > 0$,

$$z := \omega + \varepsilon, \qquad P_{j,\varepsilon} := P_j(z - \varepsilon).$$

That is, we have to show

$$\forall\ 0 < \varepsilon \ll 1\ \ \exists\, j\ \ \exists\, z_j,\ P_{j,\varepsilon}(z_j) = 0 :\ \ \Re z_j \geq 0. \quad (15)$$

To prove (15) we start with computing

$$P_{j,\varepsilon} = q_4 z^4 + q_3 z^3 + q_2 z^2 + q_1 z + q_0$$

where

$$\begin{aligned} q_4 &= \tau, \\ q_3 &= -4\tau\varepsilon + 1, \\ q_2 &= 6\tau\varepsilon^2 - 3\varepsilon + \lambda_j^\alpha + \tau(\lambda_j + \lambda_j^{2\beta}), \\ q_1 &= -4\tau\varepsilon^3 + 3\varepsilon^2 - 2\left(\lambda_j^\alpha + \tau(\lambda_j + \lambda_j^{2\beta})\right)\varepsilon \\ &\quad + \lambda_j + \lambda_j^{2\beta}, \\ q_0 &= \tau\varepsilon^4 - \varepsilon^3 + \left(\lambda_j^\alpha + \tau(\lambda_j + \lambda_j^{2\beta})\right)\varepsilon^2 \\ &\quad - (\lambda_j + \lambda_j^{2\beta})\varepsilon + \lambda_j^{1+\alpha}. \end{aligned}$$

Since $\lambda_j \geq \lambda_1 > 0$, there is $0 < \varepsilon_0 < \frac{1}{4\tau}$ such that for all $0 < \varepsilon \leq \varepsilon_0$ the coefficients $q_4, \ldots, q_0$ are positive. So we assume w.l.o.g. from now on that $0 < \varepsilon \leq \varepsilon_0 < \frac{1}{4\tau}$.

We use the Hurwitz criterion [14]: Let

$$\mathbb{H}^j := \begin{pmatrix} q_3 & q_4 & 0 & 0 \\ q_1 & q_2 & q_3 & q_4 \\ 0 & q_0 & q_1 & q_2 \\ 0 & 0 & 0 & q_0 \end{pmatrix}$$

denote the Hurwitz matrix associated to the polynomial $P_{j,\varepsilon}$. Then (15) is fulfilled if we find, for given small $\varepsilon > 0$, a (sufficiently large) index j such that one of the principal minors of $\mathbb{H}^j$ is not positive. The principal minors are given by the determinants $\det D_m^j$ of the matrices D_m^j, for $m = 1, 2, 3, 4$, where D_m^j denotes the upper left square submatrix of $\mathbb{H}^j$ consisting of the elements $\mathbb{H}_{11}^j, \ldots, \mathbb{H}_{mm}^j$.

Since

$$\det D_1^j = q_3 > 0 \quad \text{and} \quad \det D_4^j = q_0 \det D_3^j,$$

with positive q_0, it remains to prove that

$$\text{either}\ \ \det D_2^j \leq 0 \quad \text{or}\ \ \det D_3^j \leq 0,$$

for some (sufficiently large) j.

The set of parameters (β, α) for which we have to prove this, will be divided into two subsets, the first one, where $\alpha < 1$, and the second one, where $\alpha = 1$ and $\frac{1}{2} < \beta \leq 1$:

Part I: $\alpha < 1$.

We have

$$\begin{aligned} \det D_2^j &= q_3 q_2 - q_4 q_1 \\ &= [1 - 4\tau\varepsilon]\cdot \\ &\quad \cdot[6\tau\varepsilon^2 - 3\varepsilon + \lambda_j^\alpha + \tau(\lambda_j + \lambda_j^{2\beta})] - \\ &\quad \tau[-4\tau\varepsilon^3 + 3\varepsilon^2 - 2(\lambda_j^\alpha + \tau(\lambda_j + \lambda_j^{2\beta}))\varepsilon + \\ &\quad \lambda_j + \lambda_j^{2\beta}] \\ &= -2\tau^2\varepsilon\lambda_j^{2\beta} - 2\tau^2\varepsilon\lambda_j + (1 - 2\tau\varepsilon)\lambda_j^\alpha - \\ &\quad 20\tau^2\varepsilon^3 + 15\tau\varepsilon^2 - 3\varepsilon \end{aligned}$$

implying

$$\det D_2^j \leq -2\tau^2\varepsilon\lambda_j + \mathcal{O}(\lambda_j^\alpha), \tag{16}$$

where we use the Landau symbol $\mathcal{O}(\lambda_j^\alpha)$ to denote a term satisfying

$$|\mathcal{O}(\lambda_j^\alpha))| \leq k_1\lambda_j^\alpha$$

with a positive constant k_1 (being independent of j, ε, τ). Thus we conclude from (16)

$$\det D_2^j < 0 \tag{17}$$

for sufficiently large j (depending on ε, τ) since $\alpha < 1$ and $\lambda_j \to \infty$ by assumption.

Part II: $\alpha = 1$, $\frac{1}{2} < \beta \leq 1$.

We compute

$$\begin{aligned}
\det D_3^j &= q_1 \det D_2^j - q_3^2 q_0 \\
&= [(1-2\tau\varepsilon)\lambda_j^{2\beta} + \mathcal{O}(\lambda_j)] \cdot \\
&\quad \cdot[-2\tau^2\varepsilon\lambda_j^{2\beta} + \mathcal{O}(\lambda_j)] - [(1-4\tau\varepsilon)^2] \cdot \\
&\quad \cdot[\lambda_j^2 + \varepsilon(\tau\varepsilon - 1)\lambda_j^{2\beta} + \mathcal{O}(\lambda_j)] \\
&= -2\tau^2\varepsilon(1-2\tau\varepsilon)\lambda_j^{4\beta} + \mathcal{O}(\lambda_j^{2\beta+1}) \\
&\leq -\tau^2\varepsilon\lambda_j^{4\beta} + \mathcal{O}(\lambda_j^{2\beta+1}).
\end{aligned}$$

implying

$$\det D_3^j < 0 \tag{18}$$

for sufficiently large j (depending on ε, τ) since $\beta > \frac{1}{2}$ implies $2 < 2\beta + 1 < 4\beta$, and since $\lambda_j \to \infty$.

With (17) and (18) we have proved (15) and hence Theorem 1. □

CONCLUSION

In modeling heat conduction, different models using Fourier's law on one hand, or using Cattaneo's law on the other hand, can lead to very similar results concerning the asymptotic behavior in time of solutions. This holds for pure heat equations (4), (5), or for thermoelasticity of second order (6).

Examples of thermoelastic plates (7) or for Timoshenko beams exhibit a different behavior: exponential stability under the Fourier law, but no exponential stability under the Cattaneo law.

We have shown that the behavior in these two special examples is typical for a large class of coupled thermoelastic systems given as abstract model in (10). This system (10) includes the models for thermoelastic plates (7), for thermoelasticity of second order (6), and for more, like viscoelastic equations.

As a result, for all models, i.e. values of the parameters (β, α), the property of exponential stability given under the Fourier law is lost under the Cattaneo law for all parameter values which are different from the pair representing thermoelasticity of second order.

As a consequence, the considerations above should trigger a discussion of the "right" modeling in heat conduction among scientists working in modeling, in fundamental analysis, and in implementations of these models in applications.

References

[1] Irmscher, T., and Racke, R., Sharp decay rates in parabolic and hyperbolic thermoelasticity, *IMA J. Appl. Math.*, Vol. 71, 2006, pp. 459-478

[2] Fernández Sare, H.D., and Racke, R., On the stability of damped Timoshenko systems – Cattaneo versus Fourier law. *Arch. Rational Mech. Anal.*, Vol. 194, 2009, 221-251

[3] Kim, J.U., On th energy decay of a linear thermoelastic bar and plate, *SIAM J. Math. Anal.*, Vol. 23, 1992, 889-899.

[4] Muñoz Rivera, J.E., and Racke, R., Smoothing properties, decay, and global existence of solutions to nonlinear coupled systems of thermoelastic type, *SIAM J. Math. Anal.*, Vol. 26, 1995, 1547-1563

[5] Liu, Z., and Zheng, S., Exponential stability of the Kirchhoff plate with thermal or viscoelastic damping, *Quart. Appl. Math.*, Vol. 53, 1997, 551-564

[6] Avalos, G., and Lasiecka, I., Exponential stability of a thermoelastic system without mechanical dissipation, *Rend. Instit. Mat. Univ. Trieste Suppl.*, Vol. 28, 1997, 1-28

[7] Quintanilla, R., and Racke, R., Addendum to: Qualitative aspects of solutions in resonators, *Arch. Mech.*, Vol. 63, 2011, pp. 429–435

[8] Fernández Sare, H.D., and Muñoz Rivera, J.E., Optimal rates of decay in 2-d thermoelasticity with second sound, *J. Math. Phys.*, Vol. 53, 073509, 2012

[9] Muñoz Rivera, J.E., and Racke, R., Large solutions and smoothing properties for nonlinear thermoelastic systems, *J. Differential Equations*, Vol. 127, 1996, 454-483

[10] Ammar Khodja, F., and Benabdallah, A., Sufficient conditions for uniform stabilization of second order equations by dynamical controllers, *Dyn. Contin. Discrete Impulsive Syst.*, Vol. 7, 2000, 207-222

[11] Hao, J., and Liu, Z., Stability of an abstract system of coupled hyperbolic and parabolic equations, Zeitschrift angew. Math. Phys. (ZAMP), Vol. 64, 2013, 1145-1159

[12] Hao, J., Liu, Z., and Yong, J., Regularity analysis for an abstract system of coupled hyperbolic and parabolic equations, *Preprint*, 2014

[13] Racke, R., Thermoelasticity with second sound – exponential stability in linear and nonlinear 1-d, *Math. Meth. Appl. Sci.*, Vol. 25, 2002, 409-441

[14] Yang, X., Generalized Form of Hurwitz-Routh criterion and Hopf bifurcation of higher order, *Appl. Math. Letters*, Vol. 15, 2002, 615-621

BOUNDARY LAYER INSTABILITIES IN NEAR-CRITICAL FLUIDS

S. Amiroudine[1,*], D. Beysens[2,3]

[1]*Université Bordeaux, Institut de Mécanique et d'Ingénierie - UMR CNRS 5295, 33607 Pessac Cedex, France.*
sakir.amiroudine@u-bordeaux.fr
[2]*Service des Basses Températures, UMR-E CEA/UJF-Grenoble 1, INAC, 38054 Grenoble Cedex 9, France.*
[3] *Physique et Mécanique des Milieux Hétérogènes, UMR 7636 CNRS - ESPCI - Université Pierre et Marie Curie - Université Paris Diderot, 10 rue Vauquelin, 75005 Paris, France.*
daniel.beysens@espci.fr
*Author for correspondence

ABSTRACT

Under weightlessness fluids subjected to high frequency vibrations (frequencies greater than the inverse of thermal and hydrodynamic timescales) can become as unstable as on Earth. Fluids near their critical point amplify these instabilities. Even minute temperature inhomogeneity in these fluids can indeed lead to large density gradients, which make them unstable under the influence of a body-force like gravity according to Rayleigh and Schwarzschild criteria. Under zero gravity, none of these two criteria applies, however the fluid is still sensitive to vibrations. In a 2-phase fluid (liquid-vapour), vibrational forces can destabilize a liquid-vapour interface leading to Faraday or frozen wave instabilities depending on the relative direction of the interface with respect to vibration direction. Similarly, vibrations can destabilize a thermal boundary layer, resulting in parametric / Rayleigh vibrational instabilities. We report here experiments performed with hydrogen under magnetic levitation near its critical point, above (1-phase region) and below (2-phase region). These experiments in particular evidence and clarify the link between frozen wave instabilities and the development of periodic liquid-vapour bands.

INTRODUCTION

Hydrodynamics of near-critical fluids have gained considerable interest since the identification of the thermo-acoustic effect which is responsible for the fast thermal equilibration of a cell heated on one boundary [1]. Transport coefficients exhibit strong deviations near the critical point [2]. Near-critical fluids are characterised by a large density like a liquid and low viscosity and high compressibility like a gas. Their thermal diffusivity goes to zero as $\varepsilon^{0.67}$ (here $\varepsilon = \frac{T - T_c}{T_c}$), whereas the isothermal compressibility, the heat capacity at constant pressure and the coefficient of thermal expansion diverge as $\varepsilon^{-1.24}$ [2]. These anomalies in thermophysical properties make near-critical fluids to be hydrodynamically and thermally very unstable. The vanishing thermal diffusivity slows down the heat transfer processes ("critical slowing down"). These singular properties imply that classical dimensionless parameters like Rayleigh or vibrational Rayleigh numbers diverge at the critical point, making the system more and more unstable and ultimately turbulent.

In space, in the absence of gravity effects, the behaviour of fluids is markedly different than on Earth. The management of fluids in such conditions (flow control, heat exchange, etc.) is often a challenge and "artificial" gravity can be looked for. It happens that fluids submitted to vibrations of "high" frequency, e.g. frequency larger than the inverse hydrodynamics times (typically thermal diffusion and viscous dissipation times) and "low" amplitude (e.g. amplitudes smaller than the sample size) exhibit convective flows that are similar to buoyancy flows under Earth gravity.

The interest of studying fluids in such conditions is manifold. Firstly, supercritical oxygen, hydrogen, and helium are already used by the space industry. Secondly, their high compressibility and slow dynamics (critical slowing down) emphasize the behavior encountered in regular fluids. Thirdly, fluids in such conditions obey universal, scaled power laws, valid for all fluids.

More specifically – and this is one of the purpose of the present paper – it was surprisingly observed in several weightless experiments that destabilization of thermal boundary layers occurred when the fluid was vibrated. We present here an overview of thermal (Rayleigh-Bénard [3-5]) and thermo-vibrational (Faraday, frozen wave) instabilities in near-critical fluids [6-8].

RAYLEIGH-BENARD INSTABILITIES

The problem that is addressed here is the stability of a horizontal supercritical fluid layer, infinite in lateral extent, heated from below in the presence of gravity. According to Rayleigh, above a critical temperature difference, the quiescent system becomes unstable and a cellular flow develops. If the variation of density with pressure is negligible compared to the

variation induced by temperature, the onset of convection is determined by the Rayleigh criterion. For the incompressible case, it writes as:

$$\mathrm{Ra} = \frac{\rho' C_p' g'}{\lambda' \nu'} \left(\frac{\partial \rho'}{\partial T'}\right)_{P'} L'^3 (T_L' - T_U') \geq \mathrm{Ra_c}$$

where T_L' and T_U' are temperatures of the lower and upper walls, respectively, C_p' λ', ρ' and ν' are specific heat at constant pressure, thermal conductivity, density and kinematic viscosity, respectively; g' is the Earth acceleration constant; $\mathrm{Ra_c}$ is the critical Rayleigh number for the onset of convection. It is equal to 657.5, 1707.8 and 1100.6, resp., depending on whether the upper and bottom boundaries are both stress-free, both solids, or whether one is solid and the other a free boundary [9].

Another limiting case which can be relevant occurs when viscosity and thermal conductivity are neglected and compressibility is taken into account; in this case, the stability criterion is the criterion due to Schwarzchild [10]:

$$\frac{\partial T'}{\partial y'} > -\frac{\rho' g'}{\beta'} (\chi_T' - \chi_S') = -\frac{g' T' \beta'}{C_p'}$$

Where y' is the spatial ordinate; χ_T' and χ_S' are the isothermal and isentropic compressibility and β' is the thermal expansion coefficient, respectively. The definition of the local Rayleigh number for accounting these two effects in compressible flows is [9, 11-12]:

$$Ra = \frac{g' L'^4 \rho' \beta' C_p' \left[\frac{(T_L' - T_U')}{L'} - \frac{g' T' \beta'}{C_p'}\right]}{\lambda' \nu'}$$

It is worthy to note that the second term of this expression (that is, the Schwarzchild term) is constant when approaching the critical point as β' and C_p' diverge with the same critical exponent. The critical temperature gradient at which convection arises is then:

$$(\delta T')_{onset} = Ra_c \frac{\lambda' \nu'}{g' L'^3 \rho' \beta' C_p'} + \frac{g' T' \beta' L'}{C_p'}$$

The second term on the right-hand side (corresponding to the adiabatic gradient) shows small variations regardless of the proximity to the critical point. The first term becomes asymptotically small close to the critical point, whereas it is dominant far from it. The critical Rayleigh number for compressible fluids is given in [12].

Figures 1 illustrates clearly that the variation of the critical $(\delta T')_{onset}$ with reduced temperature is significant. Also significant is the dependence on the thermal boundary layer thickness h'. One sees a gradual transition from adiabatic gradient condition (the Schwarzchild criterion) for inviscid, compressible fluids, near the critical point, to the Rayleigh condition corresponding to the onset of viscous convection flow far from the critical point.

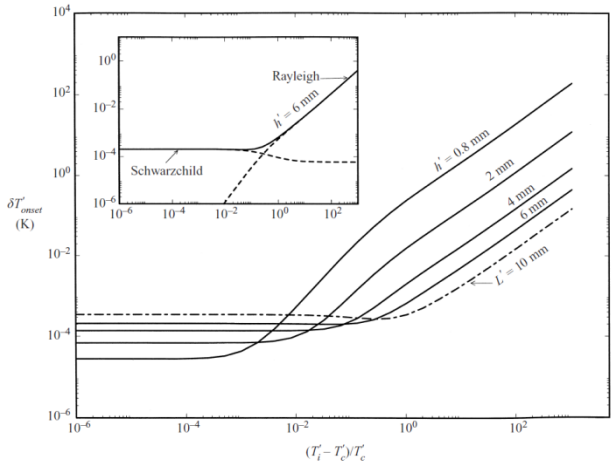

Figure 1. Critical $\delta T'_{onset}$(K) at the onset of convection as derived from Rayleigh and Schwarzchild criteria, versus reduced temperature. The characteristic length scale is the local height of the thermal boundary layer h', $0 < h' < L'$ where L' represents the total height of the cavity. The respective contributions of the Rayleigh and Schwarzchild criteria are identified and zoomed at the left top-hand side of the figure for h' = 6 mm

VIBRATIONS NEAR THE CRITICAL POINT

To carry out experimental investigation of vibration-induced instabilities close to the critical point, zero-g conditions are needed to eliminate density stratification resulting from the hyper-compressibility of the near-critical fluid.

Earlier zero-gravity experiments [13] involving vibration of a subcritical fluid enclosed in a cylindrical cavity, showed Faraday instability, square (or line close to T_c) pattern, which subsequently transformed, very near T_c, into alternate bands of liquid and vapour phases oriented perpendicularly to the vibration direction. In the supercritical region, experiments / 2D simulations [14] have evidenced Rayleigh-vibrational instability in the thermal boundary layers near the horizontal walls.

Experimental set-up

The experiments are carried out with hydrogen (H_2) as the working fluid using the facility HYLDE (HYdrogen Levitation Device [13]). The HYLDE setup uses a magnetic field generated by a cylindrical superconducting coil. Hydrogen can be levitated near the upper end of the coil where is present a near constant field gradient (1000 $T^2.m^{-1}$). HYLDE is a cryogenic facility as shown schematically in Fig. 2a. The superconducting coil made of Nb-Ti is dipped inside liquid helium at a temperature of 2.16 K and a pressure of 0.1 MPa inside the cryostat. The experimental cell is mounted inside another cryostat called anticryostat maintained under a vacuum of less than 10^{-7} mbar. Endoscopes for light source and a video camera are mounted inside the anticryostat as can be seen in Fig. 2. The positions of the endoscopes are independently adjustable. A motor driven cam based system is used to vibrate

the cell. The direction of vibration is horizontal as shown in Fig. 2b.

The experimental cells used are cuboidal cavities of size 3mm×3mm×2 mm or 7mm×7mm×7mm, made of sapphire. The uniformity of the gravity inside the cell is better than $0.025g_0$ (g_0 is the earth acceleration constant). The experiments are performed within 24 hours after filling the cell with H_2 at room temperature, thus the fluid is n-H_2. The critical point of n-H_2 is defined by: T_c = 33.19 K, p_c = 1.315 MPa, ρ_c = 30.11 kg/m^3. Hydrogen is filled inside the cell at a density within 0.2% of its critical density using a capillary tube of inner diameter 1mm. The capillary tube is fitted with a thermal switch (a small block of copper continuously cooled using liquid Helium by conduction and heated whenever required using a resistive heater). In the absence of heating the hydrogen inside the capillary tube close to the switch is in solid state thus closing the cell. To fill or empty the cell, the switch can be heated thus melting solid H_2 inside the capillary tube. The experimental cell is provided with thermal bridges (strands of copper wires connecting the bottom flange of the anticryostat, which is maintained at liquid Helium temperature, and the cell) to thermalize the fluid inside the cell. Resistive heaters in thermal contact with the cell can be used to heat the cell. Two thermometers are pasted on either side of the cell to monitor the temperature of the cell. The temperature control of the cell is achieved by using a standard PID control system. The cell is oscillated along a pivot. The centrifugal force is negligibly small in the frequency range (10-50 Hz) as 1 mm amplitude corresponds to only 1/30 radians. The cell can then be linearly vibrated in the horizontal plane at various frequencies (0 - 50 Hz) and amplitudes (0.1 mm - 1 mm).

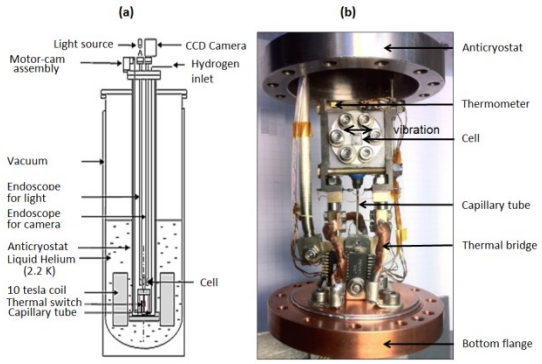

Figure 2. (a) Schematic diagram of the experimental setup HYLDE, (b) Experimental cell of size 7mm × 7mm × 7mm

Faraday waves and band pattern

The experimental cell is filled with H_2 at its critical density. Zero-gravity conditions are then established inside the cell by switching on the superconducting coil. Figure 3 shows the H_2 bubble in zero-g when the total compensation of gravity is achieved at the center of the cell relatively far below the critical point ($\sim 100\, mK$). In the picture we can see that the vapor bubble is spherical and that the liquid surrounds it, wetting the walls of the cell. The thick dark circular portion separating the liquid and the vapor phases is the meniscus of the liquid vapor interface, appearing thick due to the partial refraction of light across it. The perfect spherical shape of the bubble inside the cell shows that the bubble is in weightlessness.

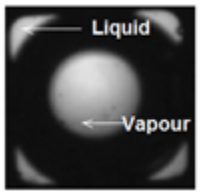

Figure 3. Hydrogen bubble in weightlessness.

Different instability mechanisms can occur for a planar fluid interface subjected to vibrations, depending on their mutual orientation. Under vibrations normal to the interface, a parametric instability in the form of Faraday waves can develop. Under vibrations tangential to the interface, a Kelvin-Helmholtz (K-H) type of instability can appear. When the bubble is subjected to vibration, some parts of its surface turn out to be nearly perpendicular to the vibration direction and the other parts are parallel to the vibration direction. In this situation both Faraday and K-H instabilities could arise at different parts of the bubble surface. However, the conditions for the excitation of these two types of instability are different; they would thus develop in different parameter ranges. As a matter of fact, vibration experiments close to the critical point are able to show both types of instabilities.

Figure 4 shows the results of the experiments carried out on HYLDE setup using the cubical cell of size 7 mm for gravity levels between 0.2g and 0g, when the temperature of the cell goes from T_c – 103 mK to T_c – 5 mK for frequency f = 40 Hz and amplitude a = 0.26 mm. As one approaches the critical point, the surface tension of the liquid-vapor interface and the liquid-vapor density difference decrease. This decrease renders the interface more flexible, resulting in the decrease in the wavelength of the instability. This can be observed very clearly in Fig. 4 where the number of Faraday fingers increases from 3 at 103 mK to 9 fingers at 12 mK. Nevertheless, the wavelength does not decrease indefinitely due to the viscous dissipation. Close to the critical point a saturation to a finite value occurs while the square pattern transforms itself into a line pattern [8] (see Fig. 4).

When the temperature of the cell reaches sufficiently close to the critical point, the horizontal fingers of Faraday wave instability fade away and the liquid and the vapor phases start organizing themselves as alternate vertical bands (see last picture of Fig. 4). The transition of the Faraday waves into vertical bands clearly indicates a competition between two different physical phenomena close to the critical point. While one mechanism is predominant far from the critical point, the other mechanism is predominant close to it. This is reflected by the fact that there exists a small transition region in which the Faraday waves start weakening out while the band pattern gain importance. Figure 4 clearly shows this transition from the Faraday waves to the band pattern. It can be seen that while

Faraday waves start to fade away as the temperature is increased, thin line-like structures start forming. Then, the Faraday waves completely disappear and the band pattern becomes predominant.

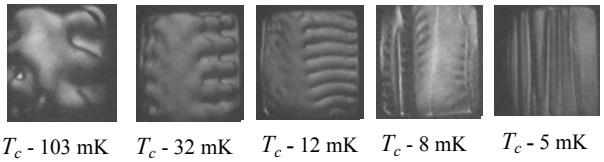

Figure 4. Transformation of Faraday square pattern (T_c-103mK, T_c-32mK) into line pattern (T_c-12mK) and eventually (T_c-8mK, T_c-5mK) into alternate bands of liquid-vapour phases as the critical temperature T_c is approached. (Cubic cell of 3mm filled with H_2 under horizontal vibration f = 40 Hz and a = 0.26 mm).

Figure 5 plots the critical point proximity T_c-T against the vibrational velocity ($a\omega$) for the coexistence of the Faraday and band pattern. The solid line indicates the temperature proximity at which the band pattern first appears when the cell is heated from a temperature below T_c towards T_c. Similarly, the dashed line gives the temperature proximity at which the Faraday wave instability ceases to exist, again when the cell is heated from a temperature below T_c towards T_c. It can be seen that at higher vibrational velocities Faraday waves disappear or band pattern first appear at temperature closer to the critical point. There exists a crossover between the two lines for values of $a\omega$ smaller than around 0.04 m/s, the value above which there exists a narrow band of temperature range where the two patterns (Faraday and band patterns) coexist.

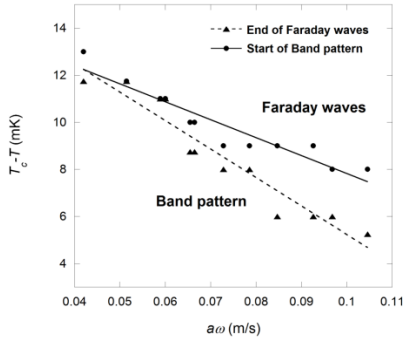

Figure 5. Transition from Faraday wave instability to band pattern. The symbols are the experimental points while the solid and dotted lines are the linear fit of the data points.

Frozen-wave instability

Under finite, steady acceleration g, a frozen wave instability can develop [15]. It is characterized by a wave pattern immobile in the cell reference frame. Magnetic levitation gives a unique opportunity to vary the magnetic force and thus the gravity compensation. Figure 6 shows such frozen waves observed in the cubic cell of side 7mm for vibration a = 0.83 mm and f = 25 Hz and for three different gravity levels g = $0.18g_0$, 0.1 g_0 and 0.05 g_0 as the cell is slowly heated towards the critical point. It was observed that the wave pattern does not change phase with time, clearly showing that the pattern corresponds indeed to the frozen wave instability. It can be seen that the wavelength of the instability decreases as the critical point is approached. This is because the surface tension of the liquid-vapor interface and the liquid vapor density difference vanish, making the interface more and more flexible. It can generally be observed that the amplitude of the frozen wave pattern is more or less constant and is not dependent on the temperature proximity.

For a given $T_c - T$ and velocity $a\omega$, it can be seen that the wavelength λ increases with a decrease in gravitational acceleration. This can be observed from the images corresponding to around 13 mK for $0.18g_0$, $0.1g_0$ and $0.05g_0$ in Fig. 6.

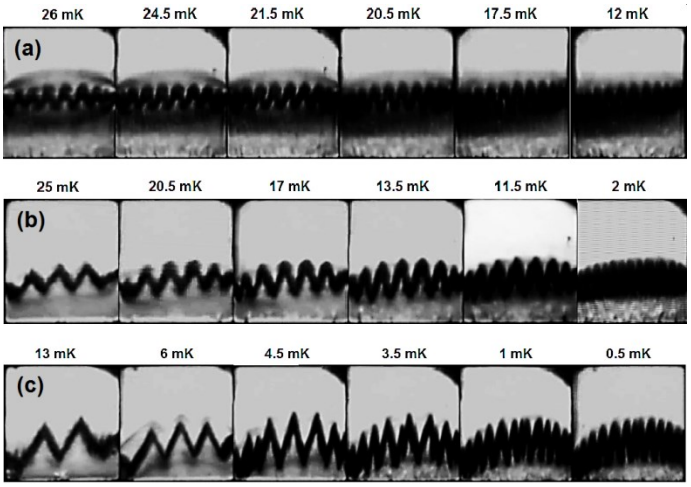

Figure 6. Frozen wave instability for the vibration case a = 0.83 mm and f = 25 Hz (7mm cell) for gravity levels: (a) $0.18g_0$, (b) $0.1g_0$ and (c) $0.05g_0$.

Under zero-g conditions, the vapor bubble is initially spherical, surrounded by its liquid. Under vibration, at a particular proximity to the critical point alternate layers (band pattern) of liquid and vapor phases aligned perpendicular to the direction of vibration occurs (see Fig. 4). The band pattern shares some similarities with frozen waves under non-zero gravity fields. Similar to the frozen wave pattern, band pattern cannot occur for higher liquid-vapor density differences. Both frozen waves and band pattern occur at temperatures very close to the critical point. In both types of phenomena the waves are frozen with time. Thus there is a probability that the band pattern we observe in zero-g experiments very close to the critical point are actually frozen waves in zero-g.

Figure 7 shows the wave pattern of the frozen wave instability for gravity varying from $0.18g_0$ to zero. The results are shown for two vibration amplitude a = 0.53 mm and frequency 25 Hz. The wave patterns are not at the same temperature, which does not matter as the wave amplitude is only weakly T-T_c dependent. It can be seen that the amplitude of the frozen waves increases quite remarkably as gravity is reduced, to

reach the sample size at some weak g-value. We thus presume that this latter configuration corresponds to the zero-g case where the observed band pattern would correspond to the frozen wave pattern at finite g.
It is important to note that the frozen wave instability is associated with a threshold (with respect to the vibration parameters a and ω) while the band pattern should have no threshold as has been observed in numerical calculations for semi-infinite layers of fluids [16].

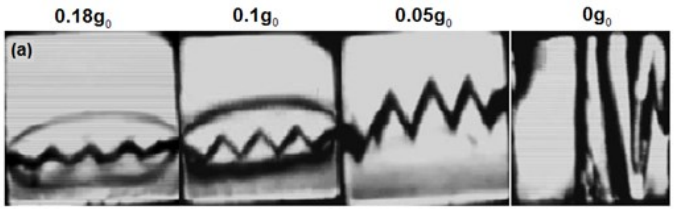

Figure 7. Frozen wave amplitude for various gravity levels with a = 0.53 mm, f = 25 Hz. (7 mm cell; temperature is not reported as the amplitude is only weakly T-T_c dependent)

Indeed, as gravity level is reduced, the stability domain of the frozen wave instability decreases. It is thus likely that when the gravity is reduced to zero, the problem becomes completely unstable, with zero threshold.

Two-dimensional numerical simulations

In the supercritical region, 2D numerical simulations have been carried out for a 7 mm square cavity filled with supercritical H_2 subjected to vibration with simultaneous thermal quench (very fast temperature change $\Delta T'$) at the boundaries [8]. The governing equations comprising of the compressible Navier-Stokes equations coupled with the energy and the equation of state are discretized spatially using a staggered non-uniform mesh with higher resolution near the walls and are solved using the finite volume algorithm Simpler [17]. A first-order Euler discretization is used for time. The numerical code was successfully used for many earlier works [5, 14] and is efficient in handling hyper-compressible fluid dynamics problems.
Results showed the coexistence of three types of instabilities (Rayleigh-vibrational, parametric and corner). Figure 8 shows the results of a typical simulation case showing the parametric instability in the thermal field of the fluid oscillating at a frequency equal to half the frequency of vibration. The wavelength versus acceleration and the stability curves for two typical critical point proximities and two typical quench amplitudes demonstrate the equivalence between parametric instability in the supercritical zone and the Faraday-type instability in immiscible fluids [18]. This suggests the existence of a vanishing surface tension associated to the three types of instabilities mentioned above. The existence of such weak surface tension has been evidenced in miscible liquids [19].

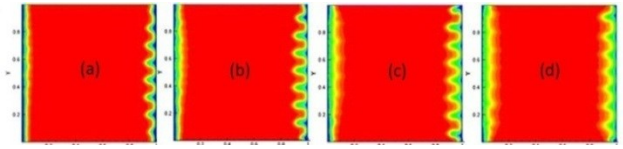

Figure 8. Parametric instability at 4 consecutive time periods at 14.4 s (a), 14.76 s (b), 15.12 s (c) and 15.48 s (d) for f = 2.78 Hz, a = 20 mm, ΔT = 100 mK and δT = 10 mK.

Figures 9a and 9b show the phase diagram of the three types of instabilities for $\Delta T'$ = 0.1K and 0.01K. It can be seen from the plots that there are zones in the stability diagram where all the instabilities are simultaneously observable. For example, the region shown by point 1 in Fig.9a indicates the region in which corner, Rayleigh vibrational and parametric instabilities are simultaneously observable while the region shown by 2 indicates simultaneous presence of corner instability as well as Rayleigh vibrational instability. The regions 3 and 4 indicate the presence of only Rayleigh vibrational instability or only corner instability respectively. A crossover between the Rayleigh-vibrational instabilities and the corner instabilities can be observed. The behavior of the three stability curves does not seem to change much with the change in the critical point proximity as can be observed in Fig. 9b.

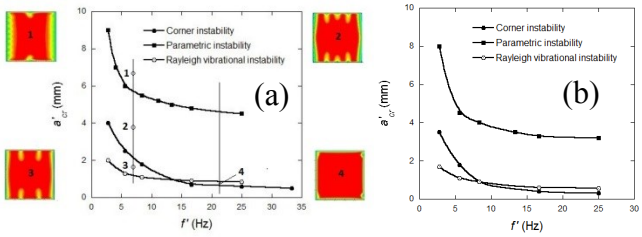

Figure 9. Stability domain for the three types of instabilities: corner (solid line with dots), parametric instability (solid line with boxes) and Rayleigh vibrational instability (solid line with circles) for (a) $\Delta T'$ = -0.1K and (b) $\Delta T'$ = -0.01K.

Comparing these three kinds of instabilities, it is seen that for a given frequency of vibration, the parametric instability needs substantially higher amplitudes to appear than the two other types of instabilities. Simulations with all four isothermal walls subjected to a thermal quench showed that the parametric instability has a stabilizing effect on the Rayleigh vibrational instability. For the corner instability the stability domain reduces as the critical point is approached. Similar kind of behavior is observed for the Rayleigh-vibrational and parametric instabilities.

CONCLUSION

This paper gives an overview of thermal (Rayleigh-Bénard) and thermo-vibrational (Faraday, band-type, frozen-wave, corner) instabilities near the critical point in the sub-critical and supercritical thermodynamic regions. Due to the singular behaviour of near-critical fluids properties, quite unusual phenomena are seen: (i) Schwarzchild criterion, which exists in atmospheric layer can be valid here in mm cells for the

Rayleigh-Bénard problem; (ii) band patterns (close to the critical point) are also seen in thermo-vibrational configurations. Experimental pictures of Faraday and frozen-wave instabilities have been visualized and explained. 2D numerical simulations have also revealed these instabilities. An overall diagram has been established for two values of the proximity to the critical point. Further numerical studies are planned in the future in order to explore a direct comparison with experimental data and to cross the critical point continuously (from subcritical to supercritical states and vice-versa).

REFERENCES

[1] B. Zappoli, D. Beysens, Y. Garrabos, Heat Transfer and Related Phenomena in Supercritical Fluids, Springer-Verlag, Berlin Heidelberg, 2015.

[2] H. E. Stanley, Introduction to Phase Transitions and Critical Point Phenomena, Oxford University Press, Oxford, 1971.

[3] H. Meyer, A.B. Kogan, Onset of convection in a very compressible fluid: the transient toward steady state, Phys. Rev E, 63, 2002, 056310.

[4] Y. Chiwata and A. Onuki, Thermal Plumes and Convection in Highly Compressible Fluids, Phys. Rev. Lett., 87, 2001, 144301.

[5] S. Amiroudine, P. Bontoux, P. Larroudé, B. Gilly, B. Zappoli, Direct numerical simulation of unsteady instabilities inside a near-critical fluid layer heated from below, J. of Fluid Mech., 442, 2001, 119.

[6] G. Gandikota, S. Amiroudine, D. Chatain, T. Lyubimova, and D. Beysens, Rayleigh and parametric thermo-vibrational instabilities in supercritical fluids under weightlessness, Phys. of Fluids, 25, 2013, 064103.

[7] G. Gandikota, D. Chatain, S. Amiroudine, T. Lyubimova, and D. Beysens, Frozen-wave instability in near-critical hydrogen subjected to horizontal vibration under various gravity fields, Phys. Rev. E 89, 2014, 012309.

[8] G. Gandikota, D. Chatain, S. Amiroudine, T. Lyubimova, and D. Beysens, Faraday instability in a near-critical fluid under weightlessness, Phys. Rev. E 89, 2014, 013022.

[9] Chandrasekar, S. 1961 Hydrodynamic and Hydromagnetic Stability. Clarendon Press, Oxford.

[10] Landau, L. D. & Lifschitz, E. M. 1959 Fluid Mechanics, vol. 6. Pergamon.

[11] Spiegel, E. A. 1965 Convective instability in a compressible atmosphere. I. Astrophys. J. 141, 1068.

[12] M. Gitterman, & V. A. Steinberg, Criteria for the commencement of convection in a liquid close to the critical point, High Temperature, USSR 8(4), 1970, 754.

[13] D. Beysens, Y. Garrabos, D. Chatain and P. Evesque, Phase transition under forced vibrations in critical CO_2, Europhys. Lett., 86, 2009 16003.

[14] S.Amiroudine, D.Beysens, Thermovibrational instability in supercritical fluids under weightlessness, Phys. Rev. E,78, 2008, 036323.

[15] R. Wunenburger, D. Chatain, Y. Garrabos and D. Beysens, Magnetic compensation of gravity forces in (p-) hydrogen near its critical point: Application to weightless conditions, Phys. Rev. E 62, 2000, 469.

[16] T. Lyubimova, private communication (2014).

[17] S. Patankar, *Numerical Heat Transfer and Fluid Flows*, (McGraw Hill, New York, 1980).

[18] Kumar, K. & Tuckerman, L. S., Parametric instability of the interface between two fluids. J. Fluid Mech., 1994, 329, 49–68.

[19] L. Lacaze, P. Guenoun, D. Beysens, M. Delsanti, P. Petitjeans, P. Kurowski1, Transient surface tension in miscible liquids, Phys. Rev. E 82, 2010, 041606.

COUPLED MULTI-SOLVER METHODOLOGY AND APPLICATION TO A LARGE SCALE INDUSTRIAL FURNACE

KHOURY R.*, GHANNAM B. , KHOURY K. and Nemer M.
*Author for correspondence
Centre for energy efficiency of systems(CES),
MINES ParisTech, PSL Research Universtiy,
Palaiseau, 91120,
France
E-mail: roukoz.el_khoury@mines-paristech.fr

ABSTRACT

In most large scale industrial furnaces, transient heat treatments involving all modes of heat transfer occur over long periods of time. In such installations, radiation is tightly coupled with conduction and convection. Transient Computational Fluid Dynamics (CFD), extended to solve radiation and solid conduction, requires considerable computing resources and long CPU processing time to simulate such systems. This paper deals with the transient multi-physical and multi-mesh simulation of large scale industrial thermal systems. The Component Interaction Network (CIN), which belongs to the dynamic thermal simulation methods, is used to finely resolve the 3D coupled transient conduction and radiation problem. Steady-state CFD is used to solve the air flow characteristics including turbulence and buoyancy effects. The two modelling approaches are linked via a newly proposed coupling method that allows the incorporation of the fluid flow effects in the thermal model by field averaging. The proposed methodology takes advantage of the speed of CIN for conduction and radiation simulation while minimizing assumptions on the flow field using a certain number of CFD solutions. A large scale industrial aluminium brazing furnace during its 2 hours cool down cycle is simulated using the proposed coupling methodology and the results are experimentally validated. While classical CFD-type multi-physical transient simulation of such large scale installations over long periods of time (two hours) is very expensive, the proposed methodology allows the determination of the 3D transient temperature field inside the furnace for the whole cool down cycle in just under 30 hours on a regular work-station.

INTRODUCTION

In high temperature industrial applications, radiation, conduction and turbulent fluid flow may simultaneously interact in various proportions, in a transient and coupled manner. Advances in computing power, numerical methods and algorithms render realistic modelling of complex three dimensional thermal problems feasible even on personal computers. Therefore industries are turning towards numerical simulation to address system level heat transfer related problems. Multi-physical thermal simulation is the tool of choice when conjugate thermal interactions on a system level are considered. Different solution strategies can be adopted to achieve such simulations.

NOMENCLATURE

Letters and special characters

ρ	[Kg/m^3]	Density
c_p	[J/Kg K]	Specific heat capacity
k	[W/m K]	Thermal conductivity
S	[W]	Energy source term
$\boldsymbol{U}$	[m/s]	Velocity vector
h	[J/Kg]	Sensible enthalpy
T	[K]	Temperature
t	[s]	Time
P	[Pa]	Static pressure
$\boldsymbol{g}$	[m/s²]	Gravitational acceleration vector
$\boldsymbol{F}$	[N]	External force vector
Φ	[W]	Heat flux at interface
Q	[W]	Heat exchange between nodes
G	[W/K]	Thermal conductance between nodes
C	[J/K]	Heat capacity
$\overline{S_iS_j}$	[m²]	Total exchange area between surfaces
$\overline{s_is_j}$	[m²]	Direct exchange area or view-factor between surfaces
σ	[Kg/s^{-3}/k^{-4}]	Stefan-Boltzmann constant
m	[Kg]	Mass
$\dot{m}$	[Kg/s]	Mass flow rate
v	[m^3]	Volume
τ	[s]	Characteristic time scale
Re	[-]	Reynolds number
Gr	[-]	Grashof number
Ri	[-]	Richardson number
$\boldsymbol{\Omega}$	[-]	Physical domain
$\partial\Omega$	[-]	Boundary of the physical domain

Subscripts

h	Heat
s	Solid
f	Fluid
i, j	Counter indices
0	Reference

Acronyms

CIN	Component Interaction Network
CFD	Computational Fluid Dynamics
TEAs	Total Exchange Areas for radiative exchange
DEAs	Direct Exchange Areas
N-S	Navier-Stokes system of equations
RANS	Reynolds Averaged Navier-Stokes
PID	Proportional-Integral-Derivative

The first strategy consists in solving conduction, radiation and fluid flow equations using a single monolithic solver. Here all variables are solved simultaneously and the intrinsic coupling through the governing equations is accomplished by simultaneously advancing the whole system in time [3]. Generally, a single mesh is used for all physical domains like in [4]. This unified mathematical description of the coupled thermal system ensures convergence and accuracy, provided that the nonlinearities arising from the coupling can be solved [12]. This approach is often used with the finite element discretization technique like in [4] and [11] to address industrial problems. The formulation of a single system for a coupled thermal problem may lead to ill-conditioned or stiff matrices as pointed in [12]. Additionally, if an explicit method is used for time marching, like in [4], the time step of conduction will be the one that satisfies the CFL condition for the fluid flow problem. Such very small time steps for the whole solution drastically increase calculation times for simulations over very long periods.

The second strategy involves coupling multiple existing and well established solvers, each addressing a separate phenomenon. By splitting the problem, an additional common interface is created between the different computational domains. An additional algorithm, called the coupler, exchanges energy at this interface to achieve the coupling between the solvers. The coupled multi-solver strategy has many numerical and practical advantages over the monolithic approach. It makes a more efficient use of the available computational resources by splitting the problem into several smaller ones that can be solved efficiently. It takes advantage of available specialized solvers to address each phenomenon by its most adequate discretization technique and solution algorithms. This decreases mesh requirements by allowing non-conformal meshes at the interfaces of the computational domains. The coupled multi-solver strategy also allows the use of different time stepping schemes and time steps for every solver to minimize computational time. Finally the coupled solution can be achieved using solvers as black boxes, which is very useful when source codes are not available. The coupled multi-physical approach was first used to study the transient response of a structure to pressure shock waves in the 1970s as stated in [3]. It has been widely used ever since to address different research and engineering problems related to energy and heat transfer, from building energy simulation [18], to automotive thermal management [14] and thermo-mechanical simulation of turbines [19].

The thermal solver used in this work is based on the Component Interaction Network (CIN) for modelling steady state and transient thermal systems. CIN is a hybrid thermal modelling approach that combines zero dimensional ordinary differential equation modelling, with multi-dimensional partial differential equation modelling techniques to solve the energy equation. When modelling systems with three dimensional radiation occurring alongside conduction, radiative exchange is included in the CIN via a zonal formulation. The radiation solver uses the flux plane approximation [8] to evaluate the DEAs or view-factors. The plating algorithm [5] is then used to compute the TEAs from the view-factors in order to transfer them to the CIN thermal solver to account for radiation. The CIN approach also allows modelling of convective exchange via correlations. The CIN was used and experimentally validated on various industrial applications involving coupled radiation and conduction. It was applied in [15] to simulate the transient heat up phase of a cryogenic heat exchanger brazing furnace, [10] modelled a steel reheating furnace that uses flameless oxidation regenerative burners and [1] controlled high temperature treatment of steel slabs in a continuous reheating furnace. In [8] 3D transient radiation and conduction heat transfer inside thin glass sheets undergoing high temperature processing was modelled using CIN.

Our goal here is to efficiently simulate the transient coupled thermal behaviour of industrial installations over long periods of time where conduction radiation and fluid flow interact simultaneously. We choose to develop a coupled multi-solver approach using CIN for conduction and radiation and a commercial CFD solver for fluid flow.

Given that the transient response of the fluid flow is not of major importance in our analysis, the transient CIN thermal model is coupled to steady state CFD snap-shots using a weak pseudo-transient coupling algorithm. In conventional coupling between thermal and fluid solvers, only interfacial values are exchanged. Here we present a new methodology that allows the inclusion of three dimensional CFD results in the thermal simulation. These results are post-processed to generate a fluid network that is included in the thermal model. The resulting fluid network is made up of volumes that interact via mass flow rates and exchange heat with solid surfaces via convection. At each coupling step, the solvers update their respective coupling variables and the transient thermal simulation continues time stepping.

This paper is organized as follows: first the general coupled multi-physical thermal problem is presented with an overview of each solver and its numerical methods. The different aspects of the proposed coupling approach are then detailed. The cooling cycle of a large scale industrial aluminium brazing furnace is modelled using the proposed strategy. The simulation results are then compared to measurements done on the actual installation to show that using this computationally efficient simulation strategy, thermal management of complicated industrial furnaces can be achieved on a regular workstation.

GOVERNING EQUATIONS OF COUPLED THERMAL PROBLEMS

We consider conduction, radiation and fluid flow simultaneously occurring in a thermal system. The fluid domain Ω_F is regarded as a non-participating medium with respect to thermal radiation. At the solid-fluid interface, conduction from the solid side interacts with convection from the fluid side and radiation that was transmitted from another boundary through the fluid. All solid domains Ω_S are considered opaque made out of grey surfaces with constant radiative properties.

Fluid flow

The unsteady Navier-Stokes (N-S) system of equations for momentum and energy transport governing a Newtonian,

incompressible (low Mach number), non reacting, single species and non-participating fluid flow, are written under:

$$\nabla . \boldsymbol{U} = 0 \tag{1}$$

$$\rho \frac{\partial \boldsymbol{U}}{\partial t} = -\rho \nabla . (\boldsymbol{U} \otimes \boldsymbol{U}) - \nabla P + \mu \Delta . \boldsymbol{U} + (\rho - \rho_0)\boldsymbol{g} + \boldsymbol{F} \tag{2}$$

$$\frac{\partial \rho h}{\partial t} = -\nabla(\boldsymbol{U}\rho h) + \nabla . (k \nabla T) + S_h \tag{3}$$

The solid-fluid interface provides the appropriate boundary conditions for the fluid problem modelled by the N-S system of equations.

Combined heat conduction and thermal radiation

The transient energy equation for an opaque solid subjected to combined conduction, radiation, heat generation, and in the absence of convection is:

$$\frac{\delta(\rho c_p T)}{\delta t} - \nabla . (k \nabla T) = -\nabla . q_r + S \tag{4}$$

A major difficulty in coupled radiation-conduction heat transfer is solving for q_r. This can be overcome by using the a zonal formulation for the radiation term like in [7] and [17]. The radiative heat flux between two surfaces i and j can thus be expressed using:

$$Q_{ij,radiation} = \sigma . \overline{S_i S_j} . \left({T_i}^4 - {T_j}^4 \right) \tag{5}$$

Where $\overline{S_i S_j}$ are TEAs that represent the total fraction of radiative energy emitted by element i, and absorbed by element j. The TEAs remain unchanged for fixed geometries, and need only be calculated once if radiative properties are independent from temperature [17].

The coupled heat transfer problem

In addition to the governing equations of conduction, radiation and fluid flow, the coupling between the three heat transfer modes is mathematically modelled by the continuity of the temperature field and the normal component of the heat flux at the solid-fluid interface:

$$\begin{cases} T_S = T_F \\ \nabla . q_r - k \nabla T_S + \Phi_F = 0 \end{cases} \tag{6}$$

This system need be verified at convergence for steady state coupled simulations or at every coupling step for transient cases.

THE SOLVERS

The tree subsequent sub-sections present a brief description of each solver used in this study, its features and numerical methods.

The CIN thermal solver

The thermal solver is based on the Component Interaction Network (CIN) approach detailed in [13]. The thermal system is first decomposed into several discrete components each of which is attributed an intrinsic model governing its internal heat transfer and containing implicit information about its physical properties (ρ, c_p, k...) and its geometry (dimensions, volume, position etc...). A component can be considered as a lumped element with a single homogeneous temperature, or have a one, two or three dimensional internal model. In the latter cases, the component is meshed and the heat equation can be discretized using a finite volume or finite element method, both of which can coexist in the same thermal network [13]. The components of a CIN can interact between each other and with their surroundings via conduction, convection, radiation and/or advection.

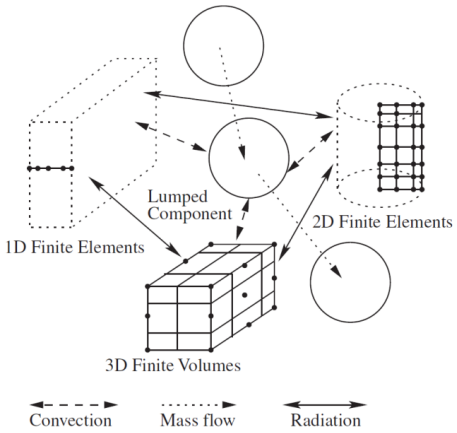

Figure 1 Illustration of the CIN for thermal systems [13].

Heat exchange between the boundary nodes of two components i and j is modelled by a thermal conductance term multiplied by the temperature difference of the nodes:

$$Q_{ij} = G_{ij}(T_i - T_j) \tag{7}$$

Each heat transfer mode has a distinct conductance term, all of which are detailed in [13]. The radiation exchange term is provided by another solver that will be presented in the next sub-section. The net heat balance on each node of the thermal network, including boundary conditions, yields a system of non-linear algebro-differential equations of conservation of energy interlinking the discretized components. This system can be written in a compact form under:

$$\mathbf{AT} + \mathbf{b} = \mathbf{C}\frac{\mathrm{d}\mathbf{T}}{\mathrm{dt}} \tag{8}$$

Where $\mathbf{T}$ is the temperature vector of unknowns, $\mathbf{b}$ the driving forces vectors, $\mathbf{A}$ and $\mathbf{C}$ two square matrices noted the exchange matrix and the heat capacity matrix respectively. Vectors $\mathbf{T}$ and $\mathbf{b}$ are of dimension m while matrices $\mathbf{A}$ and $\mathbf{C}$ are of $m \times m$. Here m is the number of isothermal nodes resulting from the discretization of the thermal network. Radiation, convection, conduction, and advection between the components of the thermal network are all explicitly present in matrix $\mathbf{A}$ under the conductances: $\bar{G}_{ij} = G_{ij,\,\mathrm{convection}} + G_{ij,\,\mathrm{conduction}} + G_{ij,\,\mathrm{radiation}}$. Equation (8) is then discretized using implicit, first or second order differentiation and solved [13].

The radiation solver

The CIN approach is not explicitly based on the geometrical surface mesh of the studied system. Nonetheless, when thermal radiation is taken into account, each component participating in the radiative exchange is attributed its own surface mesh over which the TEAs are computed by the radiation solver. For a fixed problem geometry and assuming that the radiative properties of the surfaces making up the system are independent of temperature, TEAs are computed only once as a pre-processing step and included in the global exchange matrix in the $G_{ij,\,\mathrm{radiation}}$ terms of the thermal solver. In that sense,

coupling between radiative and thermal solvers is one-way: TEAs are provided only once at the beginning of the thermal simulation.

The analytical expression of the DEA or view factor between two surfaces through a non-participating medium, expressed in angular integrals, reads:

$$\overline{S_i S_j} = \int_{\phi_1}^{\phi_2} \int_{\theta_1(\phi)}^{\theta_2(\phi)} \sin\theta \cos\theta \, d\phi d A_i \qquad (9)$$

This double integral is solved by the flux plane approximation detailed in [8] and [10] yielding the DEAs or view-factors between the thermal nodes to which is attributed the corresponding surface mesh elements. For grey radiating surfaces, TEAs are computed from the resulting DEAs using the recursive plating algorithm introduced in [5]. The plating algorithm uses a set of recursive relations that allow the TEAs to be deduced from the view-factors. Plating a surface consists in changing its emissivity from 1 to its actual value and modifying all the other TEAs accordingly, thus taking into account the diffuse multiple reflexions due to the radiative properties of the surfaces. The TEAs are obtained when all nonblack faces of the surface mesh are plated. Details and enhancements to the plating algorithm can be found in [6].

The CFD solver

The flow solver used in this study is ANSYS Fluent© which is a finite volume cell centred code that solves the N-S equations on unstructured meshes. Fluent© provides a large array of models, discretization and solution schemes for the user to choose from. They are all detailed in [2], we sum up the ones that were used in this study. Here we only present the solver setup for the solution of the steady state fluid problem. Second order central differentiation is the default scheme used for the treatment of all diffusion terms. The second order up-wind scheme is used for convective terms in all transport equations. The effect of buoyancy, due to high temperature differences in the fluid, is accounted for by the incompressible ideal gas model: ρ is considered a variable in equation (2) only, and is computed from the ideal gas relation. The body force weighted scheme is used of the discretization of the pressure gradient term to enhance stability in the presence of considerable buoyancy forces. Gradients are evaluated using the Green-Gauss node based method and the pressure-velocity coupling is treated using the coupled pseudo transient formulation to enhance convergence. Turbulence is handled by the realizable k-epsilon turbulence model introduced in [16] with enhanced wall treatment and inclusion of thermal and full buoyancy effects. Details about the implementation of this turbulence model can be found in [2].

THE COUPLING APPROACH

In steady state fluid-solid interaction, the most basic method to couple the separate solvers is to proceed by sequentially solving each sub-problem separately, while keeping fixed the interface (or boundary) values provided by the other one. The newly obtained values at the interface are then transferred to the other solver in order to re-compute its own unknowns. The process is carried out until system (6) is satisfied at the interface. Interpolation is used to map the different interfacial fields from one solver to the other if the meshes are not conforming at the interface. For transient problems, the same process is done at each coupling step.

In this work we introduce a new approach to couple CFD results to thermal simulation by creating an averaged fluid network in the thermal model. This approach allows to model transient problems more efficiently than traditional coupling methods, because it needs less CFD solutions to feed the transient thermal simulation. In the following sub-sections, the pseudo-transient temporal coupling is presented along with the field projection methods adopted between the different solvers.

The pseudo transient coupling approach

In a coupled multi-solver thermal simulation, CFD solutions account for the major CPU time. One of the major points of a new coupling strategy is to minimize the number of CFD calls while being able to account for time changing fluid boundary conditions i.e. inlet speed and temperature.

Assumptions: a significant discrepancy exists between the characteristic time scales of fluid and solid phenomena figuring in Table 1.

Table 1 Physical characteristic time-scale

Fluid motion	Fluid thermal diffusion	Solid diffusion
$\tau_f = L_{0f}/U_0$	$\tau_{f.diff} = Pr\,(L_{0f}/U_0)$	$\tau_{s.diff} = (\rho_s c_{ps} L_{0s}^2)/k_s$

The fluid dynamic and diffusive time scales, are of the same order of magnitude for air or nitrogen because their Prandtl numbers Pr are of the order of magnitude of unity. Taking aluminium as the solid, with properties at 600°C, we have $\rho_s = 2700\ \mathrm{Kg/m^3}$, $c_{ps} = 1030\ \mathrm{J/Kg.K}$, $k_s = 231\ \mathrm{W/m.K}$ while taking the same length scales for the solid and fluid domains $L_{0f} = L_{0s} = 1\mathrm{m}$ and $U_0 = 30\ \mathrm{m/s}$ we get that:

$$\tau_{s.diff} \cong 3.6 \times 10^5\ \tau_f \qquad (10)$$

This means that in certain industrial applications, the solid responds far more slowly (five orders of magnitude) to changes in dynamic thermal conditions than the fluid. Thermal transients are thus very fast in the fluid when compared to those in the solid.

Coupling strategy: since the transient response of the fluid is not of major interest, we consider that it reaches steady state instantaneously compared to the thermal evolution of the solid. This property of the two interacting physics is the cornerstone of the proposed coupling approach. Transient simulation of the conduction-radiation problem is carried out in the solid domain and steady state CFD is used to solve the fluid problem at a given moment in order to update the fluid side of the interface. This approach bridges the temporal scales of the two physics and minimizes the global CPU time of the coupling by using steady state snap shots of the fluid instead of solving the transient fluid problem. Application of a similar "pseudo-transient" coupling scheme can be found in [9].

Coupling algorithm: the above mentioned strategy can be implemented using the two general types of temporal coupling algorithms: the weak, also known as one-way or explicit coupling and the strong, also known as the two-way or implicit coupling algorithm.

In strong coupling algorithms, if the continuity conditions of system (6) at the interface are not satisfied at the end of a

coupling step, iterations are performed until they are enforced. This can be seen as iterations of a predictor-corrector scheme performed to obtain convergence of the interface conditions at each data exchange between solvers, and implies going back in time to re-evaluate the coupled solution between two coupling steps. Weak coupling algorithms on the other hand operate based on a one-way influence relation. Here, temperature variations of the solid are considered to have negligible effects on the fluid flow and iterations on the coupling steps become unnecessary to satisfy the conditions of system (6) at the interface. Even with high temperature differences between the fluid boundary and its bulk, in cases where forced convection is the main driving force of the fluid flow, very low values of the Richardson number can be achieved. This number expresses the ratio of the buoyancy term to the dynamic flow gradient, and when $Ri \ll 1$, the effects of boundary temperature on the bulk flow may be neglected.

$$Ri = \frac{Gr}{Re^2} \tag{11}$$

This is true for jets and high velocity cooling or heating flows for which loose coupling algorithms can be used without jeopardising the accuracy of the coupled solution. Figure 2 illustrates the temporal coupling between the dynamic thermal simulation and the steady state fluid solution by the weak pseudo-transient algorithm:

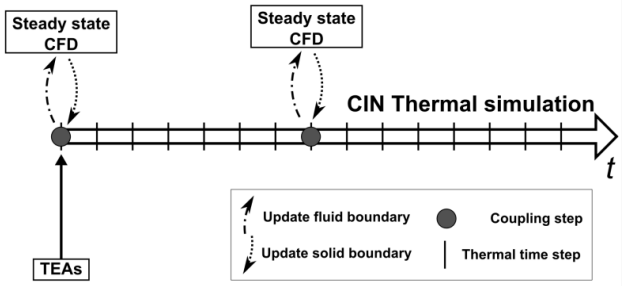

Figure 2 The CIN-CFD pseudo-transient coupling algorithm.

CIN to CFD boundary fields projection

The radiative surface mesh used for the calculation of the TEAs' and the CFD boundary mesh, are part of the interface separating the computational domains of the different solvers. In that sense, each thermal component is associated to its surface mesh on which TEAs are computed and other interfacial fields, like temperature and convective flux, are projected. The first step of any mesh based surface scalar field projection is to identify the neighbour relations between the elements of the different surface meshes. Thermal simulation surface mesh sizes are usually quite larger than the ones used for CFD simulations as pictured in Figure 3 which also illustrates the result of the neighbour search.

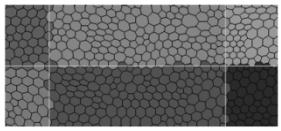

Figure 3 Polygons of a CFD surface mesh coloured by the IDs of their closest thermal surface mesh.

Exchange and interpolation techniques between the two meshes used after neighbour identification will not be discussed here. We just point that non-conservative interpolation is used to map the surface temperature field from CIN to CFD, and a conservative one is used to evaluate the convective flux on the CIN mesh that was computed on the finer CFD one.

CFD to CIN macro volume averaging

The reduction of the fluid flow information to a boundary condition in the thermal model can be a limiting factor in the simulation of large scale industrial applications. For long thermal transient evolutions, a considerable number of CFD simulations of the steady state fluid domain will be required [9]. Moreover, the interfacial exchange of information limits the possibility of including dynamic control effects (i.e. PID controllers) in the thermal model and having an instantaneous energy balance for the global installation when energy saving studies are carried out. Consequently the CFD results are sought to be included in the thermal model of the installation via three dimensional field averaging. In that sense the coupled thermal model includes a fluid network made up of volumes that exchange via mass flow rates between each other and via convection with the surfaces of the solid thermal components. This fluid network is generated from CFD simulation results of the fluid domain at a given thermal state of the structure by field averaging.

Macro volume generation: given a specified number of macro volumes (or fluid voxels) in each direction (N_x, N_y, N_z), a structured three dimensional grid is generated on the fluid domain. A geometric calculation is then performed to identify all CFD volume mesh cells that belong to each of the generated macro fluid volumes. A CFD mesh cell is included in a fluid voxel if its centroid lies inside the zone or belongs to its boundary. Each fluid voxel is thus defined by its own CFD mesh cells and its effective volume and mass are:

$$v_{voxel} = \sum_{i=0}^{\substack{i=CFD\ cells \\ in\ voxel}} v_i \tag{12}$$

$$m_{voxel} = \sum_{i=0}^{\substack{i=CFD\ cells \\ in\ voxel}} \rho_i v_i \tag{13}$$

The mass averaged enthalpy of each fluid voxel is then computed using:

$$h_{voxel} = \frac{\sum_{i=0}^{\substack{i=CFD\ cells \\ in\ voxel}} \rho_i v_i h_i}{m_{voxel}} \tag{14}$$

The result of equation (14) serves to determine the average temperature of the voxel $\bar{T}_{vox}$ computed by CFD using the enthalpy table of the fluid at the operating pressure of the installation. The effective volume of the generated voxels is used in the thermal simulation to define the components of the fluid network. We note that equations (12) through (14) take into account the presence of the solid components and avoid their inclusion in the computation of the averaged properties of the voxels.

Inter voxel mass flow rates and convection: the mass flow rates that connect the voxels in the thermal model are also computed from CFD results. To preserve the directional aspect of advection at the boundaries of each macro fluid volume, two opposite macro mass flow rates are computed from the detailed CFD ones. If Vox_1 and Vox_2 are voxels sharing a common boundary these mass flow rates are:

$$\dot{m}^{(1\to2)} = \sum_{\substack{i=CFD\ faces \\ between\ voxels \\ i=0}} \dot{m}_i^{(1\to2)} \quad (15)$$

$$\dot{m}^{(2\to1)} = \sum_{\substack{i=CFD\ faces \\ between\ voxels \\ i=0}} \dot{m}_i^{(2\to1)} \quad (16)$$

These values of the flow rates are updated at each coupling step to take into account the effect of the modified flow field in the thermal model. Having identified the fluid voxels and their boundaries, the wall heat flux is computed on the intersection between the CFD boundary faces of the voxels and the thermal surface mesh. This flux is then projected as a convective exchange on the intersecting part of the thermal mesh it and the voxel it is in contact with. Considering the surface f of a thermal component that is in contact with a fluid voxel v, the conductance of the convective exchange linking them in the thermal model reads:

$$Q_{f\to v} = G_{(f\cap v)}(T_f - T_v) \quad (17)$$

Where both T_f and T_v are determined by the transient thermal simulation if $G_{(f\cap v)}$ [W/K] and the inter-voxel mass flow rates are provided form the CFD results.

Let n_{surf} be the number of CFD boundary faces belonging to the intersection between the thermal mesh and the fluid voxel. Each of these boundary elements has a surface s, and a computed CFD thermal heat flux q^{wall} in [W/m²]. The conductance of the convective exchange at the intersection of the two meshes reads:

$$G_{(f\cap v),\,\mathrm{conv}} = \frac{\sum_{i=0}^{i=n_{surf}} (s_i . q_i^{wall})}{(T_{surf} - \overline{T}_{vox})} \quad (18)$$

Where T_{surf} is the temperature of the wall that was provided by the thermal solver at its last time step and imposed on the CFD boundary to carry out the fluid solution, and $\overline{T}_{vox}$ is the average temperature of the voxel in question computed using equation (14) and the enthalpy table of the fluid at the operating pressure. This formulation allows each voxel to be in contact with an arbitrary number of thermal surfaces and each thermal surface to be in contact with an arbitrary number of voxels.

APPLICATION TO AN INDUSTRIAL FURNACE

The aluminium brazing furnace

We consider the cooling cycle of a large scale industrial furnace used for brazing aluminium heat exchangers. The furnace is made up of a cylindrical hull containing an array of electric heaters as shown in Figure 5. The hull is 9.5 [m] long and has a diameter of 4.3 [m]. It is kept at a constant temperature during the heating and cooling cycles via a controlled water cooled jacket. The aluminium load that undergoes the heat treatment, is equipped with thermocouples at various locations in order to track its temperature. When introduced inside the furnace the load follows a specific heat-up profile via radiation under vacuum up to 600°C approximately. At the end of the heat-up cycle, gaseous nitrogen, at 200°C approximately, is injected through nozzles present inside the furnace to cool down the load at a prescribed cooling rate. The cooling rate is tracked by the readings of the different thermocouples and controlled by modulating the injection velocity of nitrogen. The heat-up cycle of the installation was modelled in [15], here we are interested in its cooling phase. The considered load is 7.5 [m] long, 1.5[m] wide and 1.8 [m] high. Cooling is controlled from peak heating temperature down to a certain level at which the metallurgical transformations inside the load stop. This results in a two-hour cooling phase.

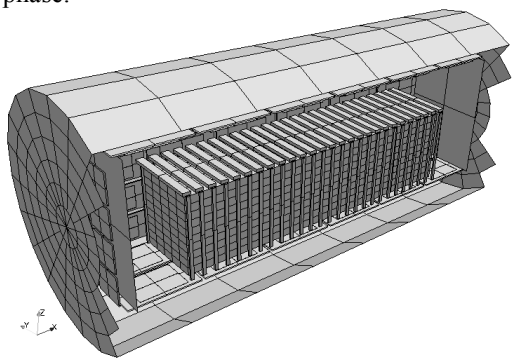

Figure 4 A cut away of the external hull of the furnace.

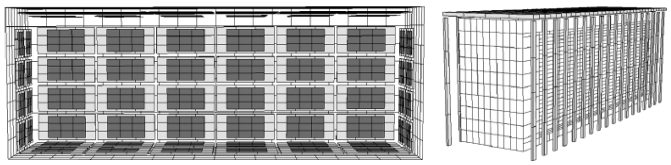

(a) (b)

Figure 5 The internals of the brazing furnace: (a) cross section of empty furnace; (b) the added load.

The coupled CIN/CFD simulation of the installation

Figure 4, Figure 5(a) and Figure 5(b) show the surface mesh that is used to carry out the radiation calculation before feeding its results to the thermal solver. The total number of gray radiating faces is 2750 with emissivities ranging from 0.15 to 0.95. The gray total exchange areas are computed in under two minutes on a regular workstation.

The thermal model is made up of a constant temperature volume for the cylindrical hull (due to temperature control), homogeneous volumes for the thin electrical heaters and a specially conceived three dimensional conduction model for the core the load. The initial temperatures for the cooling cycle are obtained at the end of the heat-up phase. The nitrogen that cools down the load is modelled by 15x10x9 fluid volumes in the X,Y and Z directions respectively. The thermal model is thus made up of 1500 variables and 15600 exchanges approximately. The simulation is carried out on a two hour period with a constant time step of one minute.

The CFD model on the other hand is symmetrical. It is made up of nine million hexahedral volume cells with 45000 boundary cells approximately. Figure 6 pictures the surface mesh of the CFD model of the installation.

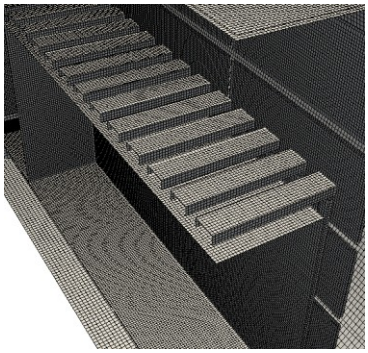

Figure 6 Surface mesh of the CFD model showing the electric heaters and the load.

All thermal boundary conditions of the CFD model are controlled by the thermal solver. Inlet nitrogen nozzle velocities and temperatures are function of the thermal simulation time. The weak pseudo-transient coupling algorithm is used to couple the thermal and fluid solvers. The different coupling moments are chosen to correspond to major changes in the blowing inlet velocity due to cooling rate control. The different coupling steps with their respective inlet velocities and temperatures figure in Table 2. Nozzle velocities vary by a factor of 4 throughout the cooling phase. Between two coupling moments, the updated inter-voxel mass flow rates and convective exchanges are kept constant up to the next coupling. At the end of the first run of the coupled simulation, the thermal solver re-simulates the cool down using interpolated fluid values at each moment of the simulation without re-computing the fluid flow.

Table 2 Coupling steps of the cooling cycle

Coupling time in minutes	Scaled inlet nitrogen velocity	Scaled inlet nitrogen temperature
0	0.25	0.833
30	0.5	0.583
60	0.75	0.517
80	1.00	0.517
120	1.00	0.517

SIMULATION RESULTS COMPARED TO MEASUREMENTS

Here we compare the readings of the thermocouple at different locations on the load with their corresponding results of the coupled simulation. Due to symmetry, the readings of eight thermocouples located on a single side of the load are chosen for the comparison. The locations of the thermocouples at which simulation results are compared to experimental measurements are indicated by dotted circles on the figures showing the relative position of the load to the electrical heaters in the furnace. Results are presented in the following figures:

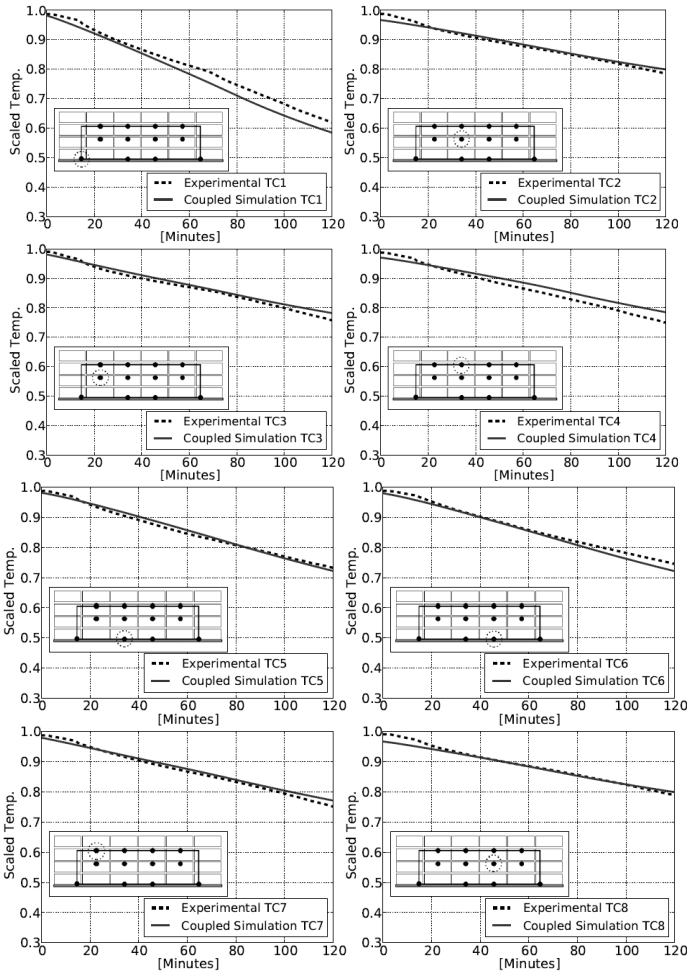

Figure 7 Comparison of cooling cycle simulation results with experimental measurement at different locations on the load.

DISCUSSION

Given the operating conditions of the installation for a specific load configuration, the goal is to evaluate the capacity of the proposed simulation approach to reproduce its thermal behaviour while maintaining a small CPU time. Simulation results are in very good agreement with the experimental measurements for most of the thermocouples. A slight difference can be noticed at the beginning of the cooling cycle: the first 5 to10 minutes. This is due to the initial conditions of the thermal model that do not perfectly match the measurements. Moreover, at the beginning of the cooling phase, nitrogen slowly fills up the furnace that was under vacuum during heat-up, and flows inside the load. These physical phenomena are not accounted for by the model because we consider that the hull instantaneously fills up with nitrogen that cannot flow inside the load.

The total running time of the coupled simulation with five coupling steps is 28 hours on a regular workstation. The fluid solution runs on 4 computing threads and accounts for 89% of the computational time. It is clear that solving for transient coupled radiation, conduction and fluid flow on large scale industrial applications over long periods of time using standard CFD techniques is practically impossible using modest

computational resources. This is where the coupled multi-solver methods become advantageous.

CONCLUSION

The coupled transient heat transfer simulation problem of large scale industrial furnaces over long periods of time was considered. The coupled multi-solver, multi-mesh, fluid-structure thermal modelling approach was presented along with the radiative, conductive and fluid flow solvers. The pseudo-transient coupling algorithm between transient thermal simulation and steady state CFD was introduced and its validity justified by the characteristic time scale discrepancy that exists between the different physical phenomena. A new coupling method between CIN and CFD was proposed and presented in details. It relies on including a simplification of the fluid solution in the thermal model. The thermal boundary conditions of the CFD model as well as the fluid network characteristics (mass flow rates and convective coefficients) included in the coupled thermal model are updated at each coupling step. This proposed weak coupling method was applied on a real life large scale industrial brazing furnace. Over the two-hour cooling cycle of the industrial installation, only five coupling steps between CIN and CFD were sufficient to achieve very good agreement between the simulation results of the proposed methodology and the actual experimental measurements.

REFERENCES

[1] D. Abdo, K. El Khoury, and D. Clodic. Continuous reheat furnace modelling using a fast radiative procedure. In *The 7th European Conference of Industrial Furnaces and Boilers (INFUB)*, Porto, Portugal, April 2006.

[2] ANSYS. *ANSYS 15 Fluent Theory Guide*, 2014.

[3] K. C. Park C. A. Felippa and C. Farhat. Partitioned analysis of coupled mechanical systems. *Report No. CU-CAS-99-06*, 1999.

[4] E. Massoni T. Coupez E. Hachem, H. Digonnet. Immersed volume method for solving natural convection, conduction and radiation of a hat-shaped disk inside a 3d enclosure. *International Journal of Numerical Methods for Heat & Fluid Flow*, 22:718–741, 2012.

[5] D. K. Edwards. The plating algorithm for radiation script-f transfer factor. *Journal of Heat Transfer*, 108(1):237–238, February 1986.

[6] G. El Hitti, M. Nemer, K. El Khoury, and D. Clodic. The re-plating algorithm for radiation total exchange area calculation. *Numerical Heat Transfer, Part B: Fundamentals*, 57(2):110–125, 2010.

[7] Georges El Hitti, Grace Mouawad, Khalil El Khoury, and Maroun Nemer. Simulating the heating cycle of a thin film photovoltaic cell during rapid thermal processing. In *2010 14th International Heat Transfer Conference*, pages 663–668. American Society of Mechanical Engineers, 2010.

[8] Georges El Hitti, Maroun Nemer, Khalil El Khoury, and Denis Clodic. Modified zonal method for thin solid semi-transparent media with reflective boundary. In *ASME-JSME Thermal Engineering Summer Heat transfer Conference, Vancouver,Canada*, number HT2007-32380, pages –, Vancouver, Canada, 2007. ISBN 0-7918-3801-3 [CD-ROM].

[9] Marc-Paul Errera and Bénédicte Baqué. A quasi-dynamic procedure for coupled thermal simulations. *International Journal for Numerical Methods in Fluids*, 72(11):1183–1206, 2013.

[10] Ludovic FERRAND. *Modélisation et expérimentation des fours de réchauffage sidérurgiques équipés de brûleurs régénératifs à Oxydation sans Flamme*. PhD thesis, Ecole des Mines de Paris, 2003.

[11] E. Hachem, G. Jannoun, J. Veysset, M. Henri, R. Pierrot, I. Poitrault, E. Massoni, and T. Coupez. Modeling of heat transfer and turbulent flows inside industrial furnaces. *Simulation Modelling Practice and Theory*, 30(0):35 – 53, 2013.

[12] Björn Hübner, Elmar Walhorn, and Dieter Dinkler. A monolithic approach to fluid-structure interaction using space-time finite elements. *Computer Methods in Applied Mechanics and Engineering*, 193(23-26):2087 – 2104, 2004.

[13] K. El Khoury, G. Mouawad, G. El Hitti, and M. Nemer. The component interaction network approach for modeling of complex thermal systems. *Advances in Engineering Software*, 65(0):149 – 157, 2013.

[14] V. Kumar, S. Shendge, and S. Baskar. Underhood thermal simulation of a small passenger vehicle with rear engine compartment to evaluate and enhance radiator performance. *SAE Technical Paper*, 2010.

[15] Maroun Nemer. *Modélisation de fours de berasage sous vide et validation eexperimental,méthode de réduction du temps de brasage*. PhD thesis, Ecole des Mines de Paris, 2005.

[16] Tsan-Hsing Shih, William W. Liou, Aamir Shabbir, Zhigang Yang, and Jiang Zhu. A new k-epsilon eddy viscosity model for high reynolds number turbulent flows. *Computers & Fluids*, 24(3):227 – 238, 1995.

[17] R. Siegel and J.R. Howell. *Thermal radiation heat transfer*. Number vol. 1. Taylor & Francis, 2002.

[18] Qingyan; Klems Joseph H.; & Haves Philip. Zhai, Zhiqiang; Chen. Strategies for coupling energy simulation and computational fluid dynamics programs. *Lawrence Berkeley National Laboratory: Lawrence Berkeley National Laboratory*, 2001.

[19] Nicholas J. Hills Leo Lewis Zixiang Sun, John W. Chew and Christophe Mabilat. Coupled aerothermomechanical simulation for a turbine disk through a full transient cycle. *J. Turbomach*, 132(1):11, 2011.

SHOCK WAVE PASSAGE THROUGH A DIPHASIC MEDIUM

A. Borich*, A. Allou, J.-D. Parisse
*Author for correspondence
French alternative energies and atomic energy commission,
Cadarache Centre, building 201, St Paul Les Durance,
France
E-mail: anna.borich@cea.fr

INTRODUCTION

During the underwater explosion, petroleum-producing process or with the aim of safety level increasing on power plant station, pressure wave propagation occurs through the diphasic media. For the study of underexpended gas jet flowing into liquid it is needed to know how the droplet scratched for the liquid interacts with Mach disk. In order to avoid injecting droplet in the underexpended jet and cannot be able to control the size of the droplet which arrive to the Mach disk. The use of a moving shock wave droplet cloud with given sizes should help to determine the level of interaction between the droplets and the shock wave.

The behavior of a shock wave passing through a diphasic medium has its features and significantly differs from the one's passage through a single-phase medium. An appearance of rarefaction waves, regions with the possibility of the condensation jump, a significant changing of an intensity of the shock takes place in that case, [1,2].The passage of the shock through a gas filled by droplets of liquid can lead to their break-up or deformation, that successively influences on the flow field structure, [3]. The size and the volume fraction of the droplets were found to be the key-parameter in that process. This phenomenon is of interest It is also important in the phenomena where a detailed investigation of the dynamics and interphase interaction is required.

An experimental test has been carried out by the team of the IUSTI laboratory (Marseille University, France). The scheme of the experimental facility is shown in Figure 1. Initially, it is filled by air at room temperature. The tube consists of 3 main parts: high-pressure chamber, low pressure chamber and a 'test chamber', whereas a cloud of water droplets will be released. The size of the droplets and the height of the cloud have been set initially. The process has been visualized by the high-speed direct shadowgraph system technique. The results of that study showed a diminution of the intensity of the shock wave and the mitigation of the shock wave by the variation of the exchange surface area resulting from droplet atomization.

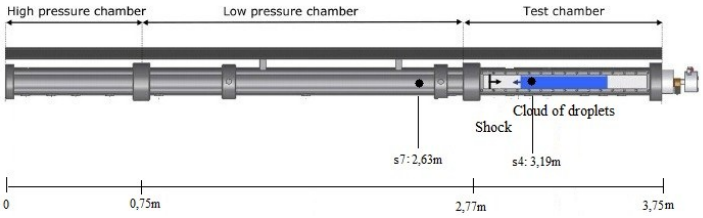

Figure 1: Experimental scheme of the shock wave passage through a diphasic medium, s4 and s7 - pressure detectors location

The aim of this study is to reproduce numerically the test mentioned above in order to apply proposed approach for a further study with another conditions. First, the numerical model proposed is validated by the comparison with the SOD test [5]. Afterwards the test with the conditions corresponding to IUSTI group's experiment has been performed. The model proposed is described below, and results obtained can be found in chapter *Results and Discussion*.

NOMENCLATURE

P	[Pa]	Pressure
ρ	[kg/m^3]	Density
v	[m/s]	Velocity
M	[-]	Mach Number
T	[K]	Temperature
γ	[-]	Specific heat capacity
S_d	[m^2]	Mean surface of the gas phase
α	[-]	Droplets volume fraction
Subscripts		
1, 2		High-pressure chamber and low-pressure chamber respectively

Numerical simulations of problem in multiphasic media have their difficulties because of the presence of large gradients in densities for the different phases. In order to obtain the solution some modification of the numerical methods, and its adaptation for the multiphasic tasks are required.

In order to respect the conditions employed in the experimental test, [4], the method of successive patching has been applied. Namely, the main computational domain has

been initially patched with a high –pressure area. The shock wave has been generated after the pressure gradient. Once the front of the shock reached a border of the area, another patching is created - the patch with a given droplet volume fraction. That way has been created in order to avoid a temporal changings of the state of the media where the shock propagates, that are caused by the initial density gradient (with the presence of droplets). Thus, the shock wave generated propagates through the non-disturbed medium in domain until it reaches the droplet filled area.

Pressure setup. The shock wave is generated according to the pressure gradient. That gradient depends on the Mach Number and can be expressed as follows, [6]:

$$\frac{P_2}{P_1} = \left(\frac{2\gamma}{\gamma+1}M^2 - \frac{\gamma-1}{\gamma+1}\right)\left[1 - \frac{\gamma-1}{\gamma+1}\left(M - \frac{1}{M}\right)\right]^{-\frac{2\gamma}{\gamma-1}}$$

Here, the gas in both areas is considered to be the same (air, heat capacity ratio γ=1.4) and with the same temperature. P_1, P_2- pressure in a low-pressure and high-pressure chamber respectively, M – Mach Number.

Droplets diameter . An influence of the size of the droplets can be estimated via the mean surface of the gas phase, S_d:

$$\boldsymbol{S_d = \sqrt[3]{\pi(6V_d)^2}}$$

Where V_d- volume of the water phase droplets.

Numerical flow solver. ANSYS Fluent code provides using of two numerical methods: pressure-based and density -based solvers The second approach is considered to be mainly used for high-speed compressible flows, while a pressure-based solver, historically, was developed for low-speed incompressible one-phase flow. However, recently both methods have been extended and reformulated to solve and operate for a wide range of flow conditions beyond their traditional or original intent,[7]. Thereby a pressure-based solver has been chosen as an operating one.

The method PISO has been employed, as the one that has proven to be robust and suitable for the problems containing discrepancies among the pressure-velocity coupling algorithms for multiphase flows. PRESTO – spatial discretization method for the pressure equation, that is considered to be more suitable for the flows involving steep pressure gradients has been used,[7]. k-e realizable model of turbulence has been chosen. The problem has been treated with the first order scheme at the beginning of the calculation with further switching to a second order.

RESULTS AND DISCUSSION

As a first step a comparison with SOD test has been performed. The conditions corresponding to a SOD case has been applied. Their values are as follows: P_1=0.1, $\rho_1 = 0.125, v_1$=0, P_2=1.0, $\rho_2 = 1.0, v_2$=0 (where ρ-density, *v*-velocity, indexes '1,2' refer to low-pressure chamber and high-pressure chamber respectively), [5].The settings of the resolution methods mentioned above are applied. The graphics shown below represent a density and a pressure distribution obtained. Here, Curves in red correspond to numerical results, curves in blue are for the results represented in G.Sod article, [5].

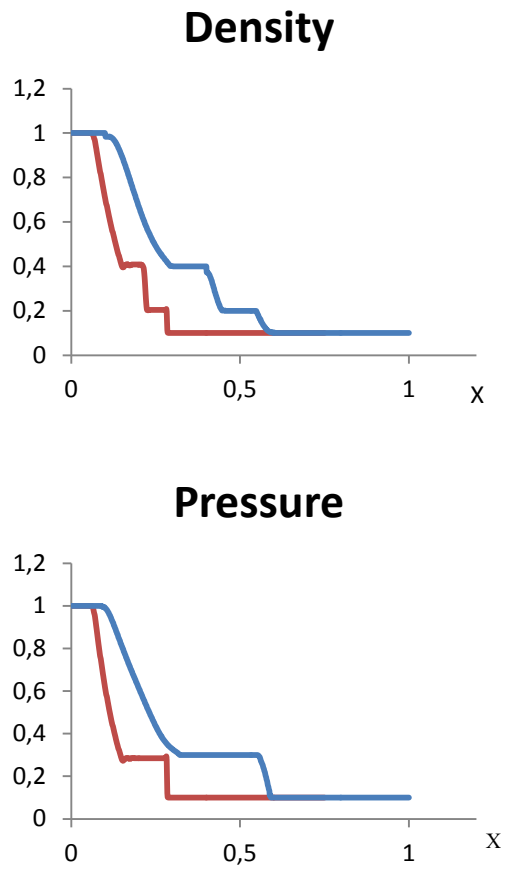

Figure 2: Pressure and density distribution for the SOD case. Curves in red correspond to numerical results, curves in blue are for the results represented in G.Sod article, [5].

The graphics obtained demonstrate qualitative agreement with a behavior of the parameters. Shock wave structure is represented correctly. That fact enables to use model proposed in order to reproduce an experimental test performed by the team of IUSTI, [4]. However, one can note some time shift. Numerically obtained results enable the feature of the shock front to propagate faster than the one represented by Sod's data. The reason for that phenomenon are currently on study.

Thus, *the second step* of that work consists in reproducing of the diphasic experimental test [4]. Necessary values for initial pressure were calculated using formula (1 –pressure set up).

Initial conditions have been calculated using formulas (1)-(2). An initial temperature is considered to be the same in all

parts of the domain. A subdomain containing droplets has been patched with the droplets volume fraction α as the front of the shock wave reached it border. The values of the parameters are given in a Table 1.

M	T, K	P_1, 10^5Pa	P_2, 10^5Pa	α
1.5	300	1	7.0	0.012

Table 1: Initial conditions

The pictures presented in Figure 3 represent pressure temporal evolution obtained and its comparison with [4] results. the data used for these graphics has been taken at the given points corresponding to the detectors location in the experiment. Figure 3 refers to a detectors s4 and s7 (in the droplets containing domain and in the part next to that respectively, its locations can be found at the figure 1). Curves in red refer to numerical results, curves in blue are for experimental data. Dotted lines represent the case of a shock propagation in diphasic medium, solid lines are for the on-phase medium case.

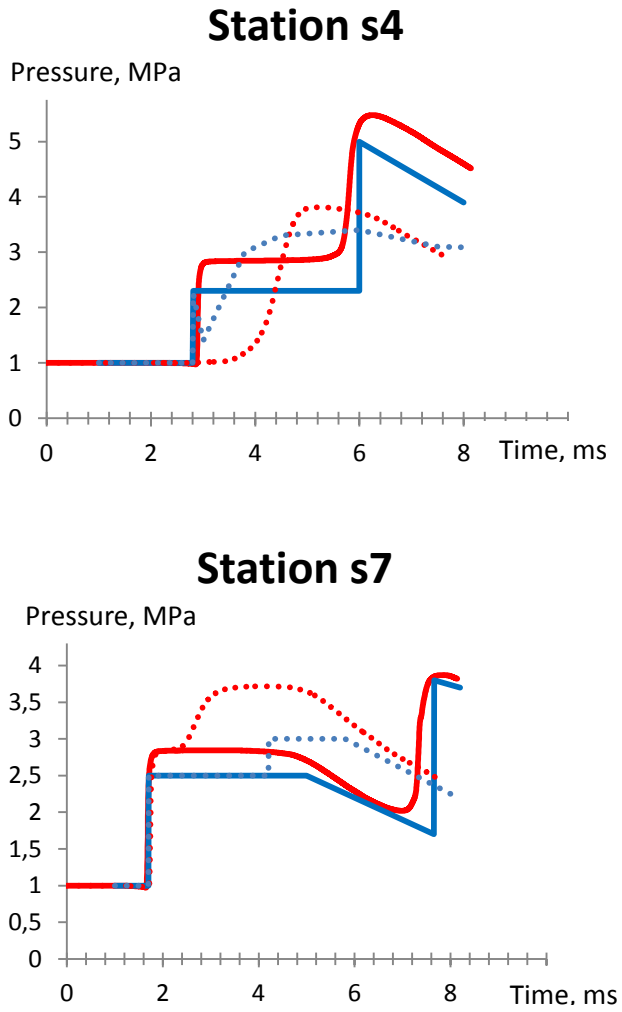

Figure 3: Comparison of pressure histories obtained with a shock wave with Mach number1.5 at the stations s4(upper figure) and s7(lower figure). Curves in red refer to numerical results, curves in blue are for experimental data. Dotted lines represent the case of the shock propagation in diphasic medium.

The qualitative behavior of the pressure curves is in accordance with experimental data, though a time lag remain. An origin of the shifts is on study now, and can be caused by the specifics of the numerical set up, or by the features of experimental facility and detectors time-start. We can note that this time lag looks very similar to the time lag appeared in test-experiments for SOD-case, discussed above. Thus the problem seems to have the same root causes.

As well it is important to note a pressure diminution of the shock wave passing through the diphasic medium, comparatively to the one-phase passage. That fact has been noticed as well in a paper [8,9]. The phenomenon can be explained by the interaction between the phases, that leads to an energy loss of the wave with its subsequent increasing, an appearance of the velocity and temperature relaxation zone. It is important to notice that numerically obtained parameters distribution repeat the experimental ones, that may indicate the ability of the approach proposed to be applied.

CONCLUSION AND FUTURE STUDY

In this work, a numerical study of the shock wave propagation through the gas medium filled with water droplets has been carried out. The test was performed for a given value of Mach number and droplets volume fraction to allow a comparison with the experimental data [4]. It was mentioned that the shock wave facing with a diphasic medium undergoes a loss of energy. And a jump in density has been noted. The results obtained shown an ability of the numerical method applied to reproduce the trend of a real experiment with a good convergence in qualitative and quantitative terms. This fact enables to apply the approach proposed for a future numerical study, namely, with different droplets volume fraction and different supersonic modes.

Based on the existent study, the size of the droplets (and its volume fraction consequently) is supposed to be a key-factor in influence on the flow structure during the shock wave passage through the diphasic medium. Thus further stage of this study is suggested to carry out a series of tests with different droplets content. As well, the flow structure may differ for the cases with higher Mach number as the slipstream of the shock will be supersonic for that case that has its effect on the processes of droplets break-ups, cavitation, and condensation and evaporation behavior. So the modes with vary flow velocity are of interest of the future works.

REFERENCES

[1] L. Landau, E.Lifshitz, Course of theoretical physics, Fluid Mechanics, Moscow 1987.

[2] Kuznetsov V.V., Nakoryakov V.E. Propagation of perturbations in a gas liquid mixture, J. Fluid Mech. 1978. V. 85, N. 1.

[3] F. Uteza, R. Saurel et al., Droplet break-up through an oblique shock wave. Shock waves Journal, 1996.

[4] A. Chauvin et al., Experimental investigation of the propagation of a planar shock wave through a two-phase gas-liquid medium, Physics of fluids 23, 113301, 2011.es Journal, 1996
[5] G. Sod, A survey of several finite difference methods for systems of nonlinear hyperbolic conservation laws, Journal of computational physics, 27, 1-31,1978.
[6] L. Lojtzansky, Fluid mechanics, Drofa, Moscow, 2003.
[7] ANSYS Fluent 14.5 Theory Guide, SAS IP, 2010.
[8] Nigmatulin R.I., Amplification and Attenuation of Shock Pulses in Gas and Vapor-Liquid Flow, Proceedings of XX IAHR Congress, Subject C, Vol.4, Moscow, 1983.
[9] Nigmatulin R.I., Amplification and Attenuation of Shock Pulses in Gas and Vapor-Liquid Flow, Proceedings of XX IAHR Congress, Subject C, Vol.4, Moscow, 1983.
[10] T.G. Yelizarova, Mathematical model and numerical methods in Fluid mechanics, Moscow, MSU, 2005.
[11] Borisov A.A., Kutateladze S.S., Nakoryakov V.E. Rarefaction waves in liquid and gas-liquid media, Ann. Rev. Fluid Mech. 1987. V. 19.
[12] G. Ostrovvskyj, Applied mechanics on heterogeneous media, St Petersburg, "Nauka", 2000.
[13] S. Someya et al, Entrained droplets in underexpanded gas jet in water, Journal of Visualization,Vol 14, 2011.
[14] V. Vshivkov, G. Lazareva, Numerical simulation of shock dynamics in bubble systems, Journal of numerical technology, 2003, Vol 8.